Distinct Stages of Stimulated FcεRI Receptor Clustering and Immobilization Are Identified through Superresolution Imaging

Sarah A. Shelby,[†] David Holowka,[†] Barbara Baird,[†] and Sarah L. Veatch[‡*]
[†]Department of Chemistry and Chemical Biology, and Field of Biophysics, Cornell University, Ithaca, NY; and [‡]Department of Biophysics, University of Michigan, Ann Arbor, MI

ABSTRACT Recent advances in fluorescence localization microscopy have made it possible to image chemically fixed and living cells at 20 nm lateral resolution. We apply this methodology to simultaneously record receptor organization and dynamics on the ventral surface of live RBL-2H3 mast cells undergoing antigen-mediated signaling. Cross-linking of IgE bound to FcεRI by multivalent antigen initiates mast cell activation, which leads to inflammatory responses physiologically. We quantify receptor organization and dynamics as cells are stimulated at room temperature (22°C). Within 2 min of antigen addition, receptor diffusion coefficients decrease by an order of magnitude, and single-particle trajectories are confined. Within 5 min of antigen addition, receptors organize into clusters containing ~100 receptors with average radii of ~70 nm. By comparing simultaneous measurements of clustering and mobility, we determine that there are two distinct stages of receptor clustering. In the first stage, which precedes stimulated Ca^{2+} mobilization, receptors slow dramatically but are not tightly clustered. In the second stage, receptors are tightly packed and confined. We find that stimulation-dependent changes in both receptor clustering and mobility can be reversed by displacing multivalent antigen with monovalent ligands, and that these changes can be modulated through enrichment or reduction in cellular cholesterol levels.

INTRODUCTION

Mast cell activation results in secretion of chemical mediators of inflammation from intracellular granules as part of the adaptive immune response, which is responsible for the symptoms of allergy. The first steps of this process occur at the plasma membrane, where antigen-specific immunoglobulin E (IgE) bound to its receptor, FcεRI, is cross-linked by soluble multivalent antigen (1,2). Cross-linking of IgE-FcεRI complexes causes signal initiation by Lyn kinase phosphorylation of immunoreceptor tyrosine-based activation motifs on FcεRI β and γ_2 subunits. The resulting tyrosine phosphorylation leads to Ca^{2+} mobilization and cellular degranulation (3). Oligomerization has readily observable effects on the spatial distribution and diffusion behavior of IgE-FcεRI. Receptors are uniformly distributed and mobile on the membrane before activation. Stimulation with antigen causes clustering of IgE-FcεRI into punctate aggregates on the cell surface and a marked decrease in receptor mobility (4,5).

Cross-linked IgE-FcεRI puncta can be visualized with conventional fluorescence microscopy. However, quantitative measurements of receptor cluster formation require subdiffraction-limited spatial resolution, comparable to the dimensions of clusters. Previous work has used a variety of experimental approaches to characterize the dynamic, antigen-induced, nanoscale reorganization of FcεRI to understand this initiation step in signaling. Receptor distributions at high spatial resolution have been studied with electron microscopy using immunogold labeling of IgE-FcεRI (6–8). In addition, dynamics of IgE-FcεRI during the time course of activation have been captured by fluorescence photobleaching recovery (FPR) (5,9,10) and fluorescence correlation spectroscopy (FCS) (11). Single-particle tracking (SPT) of individual receptors labeled with fluorescent-dye- or quantum-dot-conjugated IgE has characterized the motion of single proteins (12–14). To date, these approaches have either achieved high-resolution spatial measurements in chemically fixed systems or have measured receptor mobility in live cells using nonimaging methods or imaging without nanoscale spatial resolution.

Advances in fluorescence microscopy now enable subdiffraction imaging using photoconvertible fluorescent dyes. Superresolution techniques, including (direct) stochastic optical reconstruction microscopy (STORM/dSTORM) (15,16) and (fluorescence) photoactivation localization microscopy (PALM/FPALM) (17,18), have been used in fixed cells to quantify membrane protein distributions and clustering in other systems (19–24). Superresolution techniques in live cells capture high-resolution maps of protein distributions (25,26) in addition to diffusion information from single-molecule trajectories (27–29). Further, the use of localization microscopy for single-particle tracking methods provides improved number statistics compared to traditional single-particle tracking because the photoconversion process allows for sampling of an ensemble of receptors over the course of a single live-cell measurement. This work applies superresolution fluorescence localization microscopy, exploiting its capabilities for both high-resolution imaging and single-molecule recording of receptor diffusion. With this technique, we monitor the kinetics of clustering and mobility changes of IgE receptors in live

Submitted June 7, 2013, and accepted for publication September 9, 2013.

*Correspondence: sveatch@umich.edu

Editor: Anne Kenworthy.

0006-3495/13/11/2343/12 $2.00

http://dx.doi.org/10.1016/j.bpj.2013.09.049

rat basophil leukemia (RBL)-2H3 mast cells undergoing a stimulated immune response. We do this both by quantifying average properties of receptors and by examining the behavior of single molecules. In addition, we explore how receptor mobility and diffusion are altered by perturbations, including reversal of receptor cross-linking with monovalent hapten and modulation of the cholesterol content of cell membranes.

RESULTS AND DISCUSSION

Redistribution of IgE-FcεRI upon stimulation in live cells

Through superresolution imaging of living cells, we simultaneously observe nanometer-scale receptor organization and dynamics in real time. Fig. 1 *A* shows a representative live RBL cell that is imaged before and after the addition of multivalent antigen at room temperature under buffer conditions that both support superresolution imaging and preserve downstream functional responses (Fig. S1 in the Supporting Material). We chose to image at room temperature rather than at 37°C because key signaling stages occur at the lower temperature, although at a slower rate. These include receptor phosphorylation, Ca^{2+}mobilization, and endocytosis (11,30). Cells were sensitized by incubation with IgE antibodies specific for dinitrophenyl (DNP) and stimulated with the multivalent antigen DNP-bovine serum albumin (DNP-BSA). IgE-FcεRI complexes were fluorescently labeled by sensitizing with IgE directly conjugated to an Alexa Fluor 647 (AF647) and imaged as described in Materials and Methods in the Supporting Material. Live cell images are produced by following single-molecule trajectories in raw images, then reconstructing time-averaged images using only the first localized position in each trajectory. Each reconstructed image in Fig. 1 *A* is compiled from 2000 raw image frames acquired over 68 s of imaging time at 31 frames/s. The relatively short imaging time produces a reconstructed image that is inherently undersampled; only a fraction (estimated to be between 30% and 60%) of individual IgE proteins are represented in each image. Despite this limitation, images clearly indicate that receptors are nearly randomly organized in unstimulated cells and become more clustered in response to cross-linking by multivalent antigen.

We utilize the spatial pair correlation function as a function of radius, g(r), to quantify clustering of IgE-FcεRI complexes in reconstructed images. Pair autocorrelation functions measure the normalized probability of finding a second localized fluorophore at a given distance, r, from the average localized fluorophore. These functions are tabulated as described previously (31) and summarized in Materials and Methods in the Supporting Material. For the resulting curves, a value of 1 indicates that receptors are randomly organized. Values of >1 indicate that receptors are clustered, and the range in r over which $g(r) > 1$ is a measure of cluster size. The g(r) curves

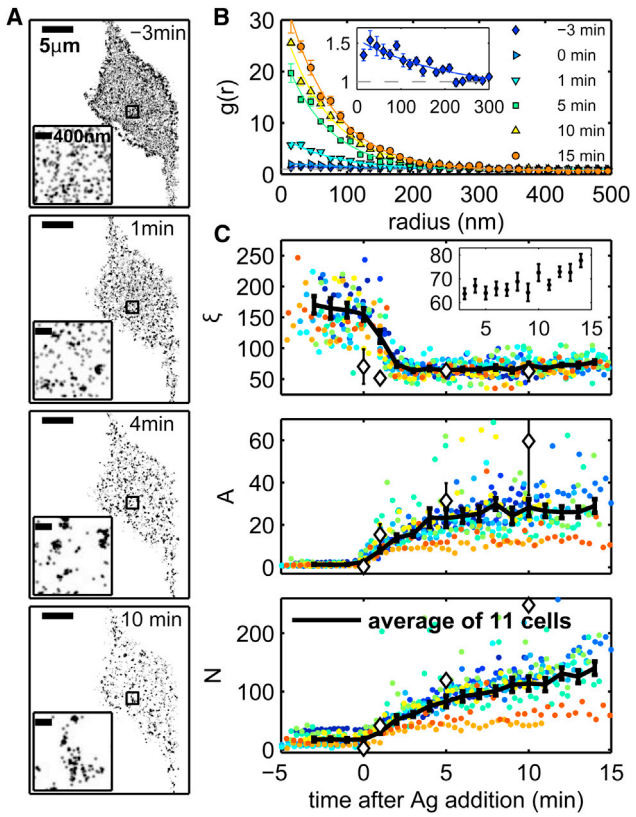

FIGURE 1 Quantitative superresolution localization microscopy imaging of IgE-FcεRI redistribution after antigen addition in live cells. (*A*) Reconstructed superresolution fluorescence localization images of an AF647-IgE-labeled living cell at various times in the stimulation sequence, where antigen (DNP-BSA, 1 μg/mL) is added at 0 min. Each image is reconstructed from 68 s of acquired data, as described in Materials and Methods (see Supporting Material). A movie showing complete time-lapse imaging of this cell is supplied in the Supporting Material. (*Insets*) Magnified images of the square regions outlined in black. (*B*) Autocorrelation functions, g(r), are calculated from reconstructed single-molecule centers acquired over 16 s, as described in Materials and Methods in the Supporting Material (*solid symbols*) and are fit to single exponentials (Eq. 1; *solid lines*). (*Inset*) The correlation function from data recorded 3 min before antigen stimulation on an expanded scale. (*C*) Correlation function parameters from 11 live-cell experiments, distinguished by different colors: the correlation length, ξ (*upper*), the correlation amplitude, A (*middle*), and the average number of correlated proteins, N (*lower*). Solid black lines indicate averages over 11 cells, and error bars represent the mean ± SE. Fit parameters extracted from two-color fixed-cell experiments are reproduced from Fig. S2, *D* and *E* and plotted for comparison in *C* as open black diamonds. (*Inset*) Average ξ for time points between 3 and 15 min after antigen addition on an expanded *y*-axis scale. To see this figure in color, go online.

shown in Fig. 1 *B* were tabulated from images reconstructed using 500 frames of raw image data acquired over 16 s. In agreement with visual observations, autocorrelation functions generated from time-resolved images show that receptors are nearly randomly distributed before antigen addition, with $g(r) \sim 1$ at all radii, and become dramatically more densely clustered after stimulation. Correlation functions measured in live cells are in good quantitative agreement with those observed in cells chemically fixed at specific

time points after stimulation (Fig. S2). Although reconstructed images of live cells are undersampled compared to fixed-cell images, as long as undersampling is random, its effects alone will not change the correlation function beyond decreasing the signal/noise ratio (31).

Measured autocorrelation functions are fit to a single exponential to extract information on average cluster size and density according to the equation

$$g_{Fit}(r) = 1 + A\exp(-r/\xi) \quad (1)$$

for $r > 20$ nm, where A is the amplitude of correlations, which is proportional to the increased density of receptors in clusters, and ξ is the correlation length, which is approximately the average cluster radius. The average number of correlated proteins (N), or the number of correlated proteins within the average cluster, is the summation of the measured g(r) over r times the average surface density of receptors, defined by the equation

$$N = \rho_{ave}\Sigma(2\pi\, r\Delta r(g(r) - 1)), \quad (2)$$

where we assume that the overall average surface density of receptors (ρ_{ave}) is 200/μm^2 (31,32). When curves are well fit to the single-exponential form given in Eq. 1 in the limit of small Δr, this sum over values of r from zero to infinity can also be written as $N = \rho_{ave}4\pi A\xi^2$. In practice, we evaluate Eq. 2 for radii between 0 and 300 nm, with $\Delta r = 15$ nm.

This quantitative analysis, averaged over 11 cells, and a summary of extracted fit parameters is shown in Fig. 1 *C*. We observe dramatic redistribution of receptors into clusters after addition of multivalent antigen with weak, long-range correlations in unstimulated cells, and strong, shorter-range correlations after antigen stimulation, consistent with previous reports in live cells (33). In unstimulated cells, we observe correlations with very low values of A and N and large values of ξ. This is further illustrated by the correlation function for unstimulated cells plotted in the inset of Fig. 1 *B*. ξ extends to ~200 nm in unstimulated live cells, whereas we observed $\xi \approx 80$ nm in chemically fixed cells (Fig. S2). The larger ξ observed in live-cell images could arise from overcounting single molecules that are lost by our tracking algorithm, lateral motion of any correlated structures observed during data collection, or, possibly, the fact that live cells were imaged at room temperature whereas chemically fixed cells were incubated at 37°C.

We observe time-dependent increases in A and N during the first 5 min after antigen addition. After this time, the correlation amplitude, A, remains constant, the average number of correlated proteins, N, continues to increase at a slower rate, and the correlation length, ξ, slowly increases (Fig. 1 *C upper*, *inset*). The average ξ decreases within 3 min of antigen addition to ~70 nm, in good agreement with ξ in stimulated fixed cells (Fig. 1 *C*, *diamonds*). The continuous decrease in ξ soon after antigen addition likely indicates the increasing presence of small and dense clusters in a background of larger more diffuse structure, as suggested by the image reconstructed from data acquired 1 min after antigen addition in Fig. 1 *A*, although we do not attempt to resolve two distinct components in g(r).

Our choice to quantify single-color live-cell images using autocorrelations relies on the assumption that live-cell superresolution images are not greatly affected by artifacts associated with overcounting single receptors. We expect this to be the case because individual fluorescently labeled receptors will typically diffuse over distances much larger than correlated structures with dimensions of several hundred nanometers or less during the time that a fluorescent molecule labeling an individual receptor remains in the dark state. This assumption may not be valid in stimulated cells, where receptors may become confined within densely cross-linked clusters, and the same receptor may be counted multiple times within a single cluster. If there is a contribution to correlation functions from overcounting, our reported results would lead to an overestimate of A. However, the values of A we observe from autocorrelation functions in live cells are systematically lower than values of A extracted from cross-correlation functions in fixed cells (Fig. 1 *C*, *black diamonds*), which are not affected by overcounting artifacts. This supports the assumption that overcounting does not affect correlation functions throughout the time course of imaging.

Our results using chemically fixed cells (Fig. S2) are consistent with and complementary to our live cell measurements in several regards. Agreement of A and N between fixed and live cells at early stimulation time points indicates that clustering occurs to approximately the same extent, although at a somewhat slower rate, in cells stimulated at room temperature compared to those stimulated at 37°C. Further, results from fixed-cell experiments demonstrate that receptors are not clustered before stimulation. This result is important in the context of our live-cell experiments, because small and highly mobile clusters that diffuse much farther than their size over a typical image acquisition time would not be detected by our live-cell quantification methods.

Mobility of IgE-FcεRI in live-cell measurements

The majority of individual fluorophores remain in a fluorescent state for multiple sequential frames, and we track these probes to form trajectories from localizations of the protein in time and space (see Materials and Methods in the Supporting Material). Visual inspection of trajectories obtained from 16 s of acquired data in unstimulated and stimulated cells suggests that IgE-FcεRI diffusion is relatively unconstrained before stimulation and that mobility decreases significantly after antigen addition (Fig. 2 *A*). Trajectories are quantified by tabulating the mean-square displacement (MSD) as a function of time interval (τ). Several representative curves are calculated by averaging MSD(τ) values

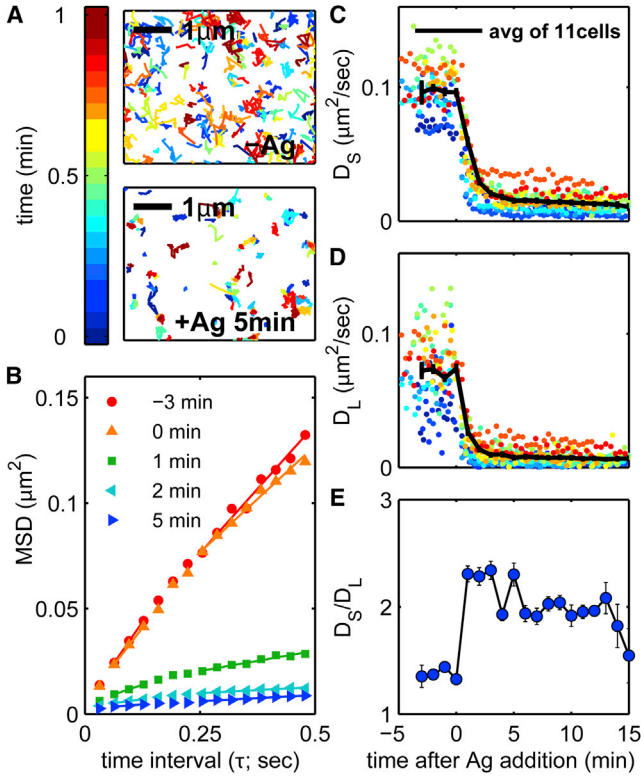

FIGURE 2 Antigen stimulation leads to slower and more confined diffusion of IgE-FcεRI receptor complexes. (A) Single-molecule trajectories of IgE-FcεRI complexes on the surface of cells under TIRF illumination before (−Ag) and after (+Ag) stimulation with 1 μg/mL DNP-BSA for 5 min. Tracks shown are accumulated over 1 min, only tracks observed for five or more frames (0.16 s) are displayed, and coloring from blue to red indicates the relative time at which a single probe was observed within the 1 min time frame. (*B*) MSD curves are generated by averaging over all tracks observed within a 500 frame (16 s) time period at the times during antigen stimulation indicated, as described in Materials and Methods in the Supporting Material. MSD curves are fit to Eqs. 3A and 3B to extract the short- and long-time diffusion coefficients D_S and D_L, respectively. (*C* and *D*) Summary of D_S (*C*) and D_L (*D*) extracted from MSD curves tabulated from single-molecule trajectories acquired over 500 frames (~20 s and variable from cell to cell) for 11 distinct cells. Error bars represent the mean ± SE of the 11 live-cell experiments. (*E*) Confinement as a function of stimulation time, as measured by D_S/D_L from the same 11 live-cell experiments. Error bars represent the mean ± SE. To see this figure in color, go online.

over all trajectories acquired within 16 s, as shown in Fig. 2 *B*. The magnitude of the average MSD(τ) decreases after stimulation, indicating reduced receptor mobility. The representative data shown in Fig. 2, *A* and *B*, are acquired from the same cell shown in Fig. 1, *A* and *B*.

In most cases, we find that the slopes of MSD(τ) are not linear, as expected for free diffusion, but instead are deflected to lower values at long τ, indicating that receptors are confined. We quantify both diffusion and confinement of IgE-FcεRI complexes as a function of stimulation time by fitting MSD(τ) to obtain both short- and long-time diffusion coefficients, D_S and D_L, respectively, which are obtained by fitting distinct time ranges of MSD(τ) curves to extract linear slopes. D_S is obtained by fitting the equation:

$$\mathrm{MSD}(\tau_{2-4}) = 4D_S\tau_{2-4} + C_S, \tag{3A}$$

where $\tau_{2\text{-}4}$ indicates the second, third, and fourth time intervals of the MSD(τ) curve, typically corresponding to roughly 50–100 ms, and C_S is the *y*-intercept of the fit that accounts for the finite localization precision of the single-molecule data. D_L is obtained by fitting the MSD curve at time intervals between 250 and 500 ms to the analogous equation,

$$\mathrm{MSD}(\tau_{250-500\mathrm{ms}}) = 4D_L\tau_{250-500\mathrm{ms}} + C_L. \tag{3B}$$

Best-fit lines to Eqs. 3A and 3B, whose slopes are proportional to the values of D_S and D_L, are shown for the representative MSD(τ) curves in Fig. 2 *B*. In addition, we quantify confinement by taking a ratio of these values, D_S/D_L. In the examples shown in Fig. 2 *B*, $D_S/D_L > 1$, indicating that receptors are confined, and this ratio increases after antigen addition.

D_S, D_L, and their ratio for IgE-FcεRI in cells undergoing signaling responses are shown in Fig. 2, *C–E*, for the same 11 cells characterized in Fig. 1. Both D_S and D_L dramatically decrease within 5 min of antigen addition. After 5 min of stimulation, D_S decreases from 0.1 to 0.02 $\mu m^2/s$ and D_L decreases from 0.075 to 0.01 $\mu m^2/s$. We also observe changes in confinement with stimulation time, as measured by D_S/D_L, which rapidly increases after stimulation before decreasing slightly at later stimulation time points.

Our measured values of D_S versus stimulation time are in agreement with similar diffusion-coefficient parameters measured previously using SPT (10,12,13,33), FCS (11), and FPR (5,9), ranging from 0.03 to 0.26 $\mu m^2/s$ before stimulation and from 0.01 to 0.16 $\mu m^2/s$ after stimulation with a multivalent antigen. Previous measurements of receptor diffusion using SPT approaches similar to ours (10,12,13,33) agree best with our observed values, where here reported values range from 0.07 to 0.1 $\mu m^2/s$ before stimulation and from 0.01 to 0.05 $\mu m^2/s$ after stimulation. Our measurements of receptor confinement are also consistent with the observation of restricted or compartmentalized diffusion in previous SPT studies of FcεRI (10,12,33). In one of these past studies, the diffusion compartments of IgE-FcεRI were reported to shift to smaller sizes upon antigen addition, accompanied by a decrease in the diffusion coefficient for movement between compartments (33). That result is consistent with the antigen-induced increase in receptor confinement measured in this study.

Correlating receptor mobility with receptor clustering

The data presented in Figs. 1 and 2 allow for direct comparison between changes in IgE-FcεRI receptor diffusion versus spatial distribution. Taken together, the results indicate that IgE-FcεRI receptor complexes have decreased

mobility (D_S and D_L) and increased confinement (D_S/D_L) that plateaus within 1–2 min after antigen addition. In contrast, the density of receptor clusters (A) increases more slowly, with the amplitude of correlations plateauing after ~5 min (Fig. 1 *C*).

To explore more directly the relationship between cluster properties and receptor mobility, we plot in Fig. 3 *A* the average short-time receptor diffusion coefficient, D_S, versus the average number of correlated proteins, N, for the stimulation time course averaged from 11 live-cell experiments (average D_S and N as a function of time are shown independently in Figs. 2 *C* and 1 *C*, respectively). Interestingly, this representation suggests two distinct regimes of receptor mobility and clustering. In the first regime, D_S decreases dramatically without a large corresponding change in N. In the second regime, receptors become increasingly clustered, without a large corresponding decrease in D_S. The crossover between regimes occurs for N between 20 and 30 and for D_S between 0.035 and 0.02 $\mu m^2/s$, which correspond to stimulation times between 1 and 1:45 min, respectively, after antigen addition.

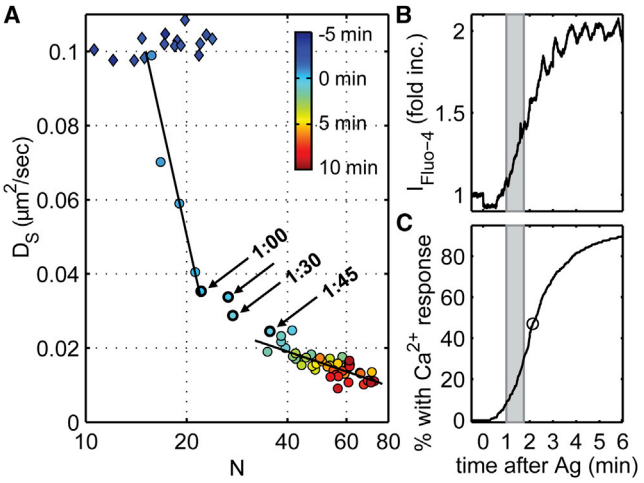

FIGURE 3 Average receptor diffusion displays two different phases of dependence on the number of proteins in the average cluster. (*A*) Average D_S (as in Fig. 2 *C*) is shown as a function of average N from the same live-cell experiments (as in Fig. 1 *C*). Each point corresponds to values of D_s and N at a given time before (*diamonds*) and after (*circles*) stimulation averaged over the 11 cells imaged, and data from individual cells are binned every 15 s to facilitate averaging. Time after the addition of antigen is indicated by the color bar. Antigen (1 μg/ml) was added after the cells were imaged for 5 min. The solid black lines represent linear fits of points between 0 and 1 min and between 1:45 and 15 min after antigen stimulation, weighted by the inverse of the mean ± SE in D_S and N for each point. Points spanning these two regimes are indicated with arrows and labeled with the time after antigen addition. (*B*) Average intensity of the cytoplasmic Ca^{2+} indicator Fluo-4 over a population of cells imaged as described in Materials and Methods in the Supporting Material. The increase in Fluo-4 intensity after antigen stimulation indicates the onset of Ca^{2+} mobilization. The time period coinciding with the timing of the transition from the first regime to the second in *A* is highlighted by the shaded region. (*C*) The cumulative distribution of cells exhibiting an initial Ca^{2+} response indicates that the majority (>90%) of cells have initial Ca^{2+} responses between 1 and 4 min after antigen stimulation. The time point when 50% of the responding cells have exhibited a Ca^{2+} response is indicated by the open circle. To see this figure in color, go online.

Interestingly, the beginning of the crossover between the two regimes shown in Fig. 3 *A* roughly coincides with the onset of Ca^{2+}signaling in RBL-2H3 cells imaged using the Ca^{2+}-sensitive dye Fluo-4 under nearly identical stimulation conditions (Fig. 3, *B* and *C*). Fluo-4 is loaded into sensitized RBL cells, and the fluorescence intensity is monitored across a field of several hundred cells as a function of stimulation time, as described in Materials and Methods (see Supporting Material). Soon after antigen addition, Fluo-4 intensity averaged over the population of cells begins to rapidly increase, with the bulk of the increase coming between 1 and 4 min (Fig. 3 *B*). There is a large cell-to-cell heterogeneity in the timing of the onset of the Ca^{2+} response, as indicated in the cumulative distribution shown in Fig. 3 *C*, with some cells initiating a response ~1 min after antigen addition under these imaging conditions. Approximately 50% of cells have experienced a Ca^{2+} response within 2:15 min. Keeping in mind this large heterogeneity and the fact that we sample only a limited number of single cells in superresolution experiments, we use the Ca^{2+} mobilization measurement as a rough indicator of the commencement of cellular signaling.

The results reported in Fig. 3 indicate that the initial, rapid decrease in D_S of IgE-FcεRI complexes is a consequence of interactions that precede Ca^{2+} mobilization, whereas the accumulation of receptors into densely packed clusters represents receptors after the onset of Ca^{2+} mobilization. This suggests that early signaling events leading to the Ca^{2+} response do not require that receptors be densely clustered or fully immobilized. This interpretation of our results is consistent with observations from previous studies that small IgE-FcεRI clusters that retain mobility can elicit a degranulation response (13), and that there is a high level of receptor tyrosine phosphorylation within the first few minutes of antigen stimulation, both at 37° and 15°C (34). In the latter study (34), receptor tyrosine phosphorylation at 15°C occurs on a timescale similar to that of the Ca^{2+} response that we measure at room temperature, as we would expect, since tyrosine phosphorylation precedes Ca^{2+} mobilization in the IgE receptor signaling cascade. The same study also demonstrated that exposure of DNP haptens on the surface of DNP-BSA is transient, and that antigen binding is dominated by cross-linking of receptors after a minute of exposure to antigen (34). This is also consistent with the idea that the immobilization and Ca^{2+} responses we observe at early stimulation times occur concurrently with the formation of small clusters, and that receptors become more heavily cross-linked at later times.

Because diffusion of cross-linked IgE-FcεRI decreases rapidly, without a corresponding large increase in N, it likely occurs as a result of IgE-FcεRI coupling to downstream signaling partners. This could be due to receptor association with other freely diffusing membrane-anchored

proteins that are not labeled in these experiments. It is possible that receptor slowing is due to slower movement between corrals defined by cortical actin, either due to mechanical occlusion of the growing signaling platforms with actin-anchored proteins (36,37), or due to increased coupling of platforms to actin-stabilized, lipid-mediated heterogeneity (38). Alternatively, the reduced mobility of receptors at early signaling stages could be a consequence of direct or indirect tethering to an immobilized component such as actin. The actin cytoskeleton has been shown to be partially responsible for the immobilization of cross-linked IgE-FcεRI (12), and it plays a role in the desensitization of receptors to antigen (39), and in internalization (40). The increasing clustering of receptors that dominates later signaling stages could be a mechanism to downregulate signaling by sequestering receptors, as occurs in B cell and T cell receptor activation (41–44). It is also possible that the observed receptor clusters represent an early stage of receptor internalization that has not progressed substantially under these conditions of stimulation time and temperature (11).

Ca^{2+} mobilization is used here as an approximate indication of the timing of the onset of cellular signaling, but consideration should be given to its direct comparison with superresolution measurements. Clustering and immobilization of IgE receptors on the ventral surface of cells could begin more slowly than Ca^{2+} mobilization because the Ca^{2+} response originates from receptors on the dorsal surface of cells, which are expected to be more accessible to antigen. This may lead to a time delay between the initiation of the Ca^{2+} response and our observation via superresolution measurements of immobilization and clustering. If this is the case, receptors on the dorsal surface may be somewhat more clustered at the onset of the Ca^{2+} response, but this would not change our conclusion that the first phase of clustering and immobilization occurs before Ca^{2+} mobilization, and the second phase occurs predominantly afterward. Ca^{2+} mobilization itself may be considered a downstream measure of the onset of signaling. Previous work has shown that receptor phosphorylation by Lyn kinase proceeds much more rapidly than Ca^{2+} mobilization (35), and thus, Ca^{2+} mobilization represents membrane interactions that initiate a broader cellular response and occur subsequent to the initiation of signaling at the level of single receptors.

Single-molecule analysis of receptor diffusion and clustering

Early and late signaling stages are also distinguished when receptors are examined as single molecules, and several representative trajectories are shown in Fig. 4 *A*. Single receptor trajectories in unstimulated cells traverse large areas. Soon after antigen is added, trajectories rapidly condense, and some receptors appear to sample multiple confined areas in single trajectories, lasting ~1 s each. After a few minutes of antigen stimulation, trajectories are compact and appear highly confined. The ensemble of single-molecule

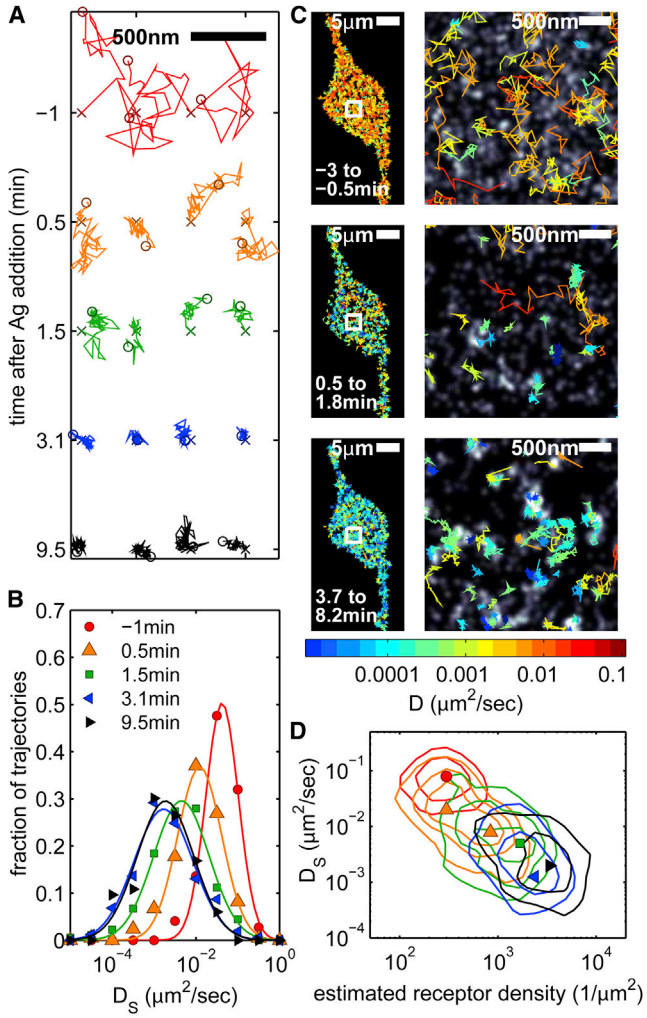

FIGURE 4 Slower and more confined diffusion of single receptors correlates with regions of high receptor density. (*A*) Examples of single-molecule trajectories are shown from the same cell in Fig. 1, *A* and *B*, Fig. 2, *A* and *B*, and Fig. 4 *C* recorded before and after antigen stimulation. The tracks shown persist for at least 0.5 s for the −1 min (unstimulated) time point and for 1 s for other time points. (*B*) Short-time diffusion coefficients (D_S) are evaluated from MSD curves tabulated from single-molecule trajectories lasting at least 0.5 s within a 16 s time period and are assembled into histograms. Histograms are normalized by the total number of tracks collected to generate each histogram. (*C*) Single-molecule trajectories persisting for at least 0.5 s are superimposed on a superresolution image reconstructed from unstimulated data (*upper*), from data acquired within 1 min of antigen addition (*middle*), and from data acquired after several minutes of stimulation. Track coloring indicates D_S for each track on a log scale from 10^{-5} $\mu m^2/s$ (*blue*) to 1 $\mu m^2/s$ (*red*). Images on the right are enlargements of the boxed regions in the images on the left. (*D*) Three-dimensional histograms of D_S versus average receptor density along trajectories lasting at least 0.5 s. The average receptor density for each trajectory is determined by averaging the pixelated grayscale values from the time-averaged reconstructed image over all positions of the trajectory and then normalizing assuming $\rho_{ave} = 200/\mu m^2$, as described in Materials and Methods in the Supporting Material.

trajectories is quantified by assembling histograms of D_S. Fig. 4 *B* shows histograms assembled using 16 s of data acquired in a single cell, which are representative of histograms obtained from other cells examined. Histograms are well described as single log-normal distributions for all time points, indicating that a single population of diffusers is resolved in these measurements. Distributions of D_S rapidly shift to lower values and broaden soon after antigen is added, stabilizing after 3 min of stimulation time. These distributions are broad, in part because diffusion coefficients are not well defined when obtained from short trajectories (45). To separate this effect from real heterogeneity, we compare measured distributions of D_S to those obtained by simulating Brownian trajectories with 16 frame (0.5 s) track length (Fig. S4). In unstimulated cells, the width of measured D_S histograms is comparable to those of simulated trajectories. In contrast, measured histograms for receptors after antigen addition are significantly broader than the simulated distributions, indicating that the membrane environment sampled by IgE-FcεRI is heterogeneous.

We also investigated how receptor diffusion correlates with the local surface density of receptors in reconstructed images. To accomplish this, we reconstructed superresolution fluorescence images as described in Materials and Methods (see Supporting Material). Representative grayscale images for a single cell at various stimulation stages are shown in Fig. 4 *C*. In these images, pixel intensity is proportional to the observed receptor density, and trajectories that persist for >0.5 s are superimposed onto this image. In the unstimulated cell (Fig. 4 *C*, *upper*), individual receptors diffuse over large areas and their mobility is not visually correlated with roughly random receptor density. Soon after antigen addition (<1 min), individual receptors appear more confined, even though the spatial distribution of receptors remains largely random (Fig. 4 *C*, *middle*). At longer times, (>5 min after antigen addition), diffusing receptors are confined to regions where receptors are densely packed (Fig. 4 *C*, *lower*).

These visual observations are quantified by calculating the average pixel intensity over the length of single-molecule trajectories persisting for >0.5 s. Three-dimensional histograms are displayed as contour plots in Fig. 4 *D* for several stimulation times. In unstimulated cells, receptor diffusion appears relatively unconstrained, and the ensemble of single molecules experiences roughly the same local environment at the frame rates used in these experiments (~30/s). This is not surprising given that receptors typically move hundreds of nanometers between observations, and over several square microns in a typical trajectory. Lipid-mediated and/or actin-generated obstacles to diffusion are expected to occur on smaller length-scales in unstimulated cells, and thus, single receptors are expected to sample a large number of local environments in a single trajectory. At long times, we observe a homogeneous but broad distribution in the D_S versus receptor density histogram in Fig. 4 *D*. This is a result of both a distribution of receptor densities in puncta and individual receptors confined to sample the local environment of single puncta over their recorded trajectories.

Soon after stimulation with antigen, histograms are elongated, extending between faster-moving receptors in a low-density local environment and slower-moving receptors in a higher-density local environment. In some cases, two peaks are observed, as indicated by the orange triangles in Fig. 4 *D*. This elongated distribution could arise from receptors sampling a heterogeneous membrane environment. We think it is more likely that this elongated distribution arises from receptors slowly exchanging between a more mobile, less aggregated state and a less mobile, cluster-associated state over the length of the trajectory, as appears to be the case from visual inspection of single trajectories (Fig. 4 *A*).

Elongated distributions in Fig. 4 *D* are observed before the onset of Ca^{2+} mobilization, and transient associations of individual receptors could represent interactions that result in signaling. This also suggests that receptor aggregation is dynamic, at least in the early signaling stages. Consistent with this interpretation, it has been shown previously that readily dissociable cross-linked receptors are primarily responsible for generating downstream signaling responses (39). Previous work has also shown that initial binding of DNP-BSA to IgE is primarily monovalent, and that cross-linking occurs slowly as DNP haptens on the receptor-bound antigen subsequently become available for binding (34). This is in good agreement with our current observations that suggest transient association of receptors with receptor clusters soon after antigen addition.

Receptor clustering, immobilization, and confinement is reversible in live cells

A monovalent DNP hapten, DNP-aminocaproyl-L-tyrosine (DCT), competes with multivalent DNP-BSA for binding to anti-DNP IgE (39). The addition of an excess of DCT after antigen stimulation reverses antigen-induced cross-linking and results in the cessation of signaling (39,46,47). The representative live-cell superresolution images in Fig. 5 *A* show uniform distribution of AF647-IgE bound to FcεRI before antigen addition, clustered IgE-FcεRI distribution after 7 min of antigen stimulation, and uniform distribution of receptors after DCT incubation for 10 min. The average time dependence of A, N, and D_S from six live-cell experiments quantifies the reversal of clustering and immobilization upon DCT exposure (Fig. 5 *B*). IgE-FcεRI clusters are dispersed on a timescale of several minutes, as shown by a decrease in A. Likewise, N and D_S recover close to prestimulation levels within 10 min of DCT addition. These data indicate that receptor immobilization is reversible and dependent on receptor cross-linking, as has been shown previously by FPR measurements that used DCT to reverse receptor immobilization (5). This reversibility demonstrates

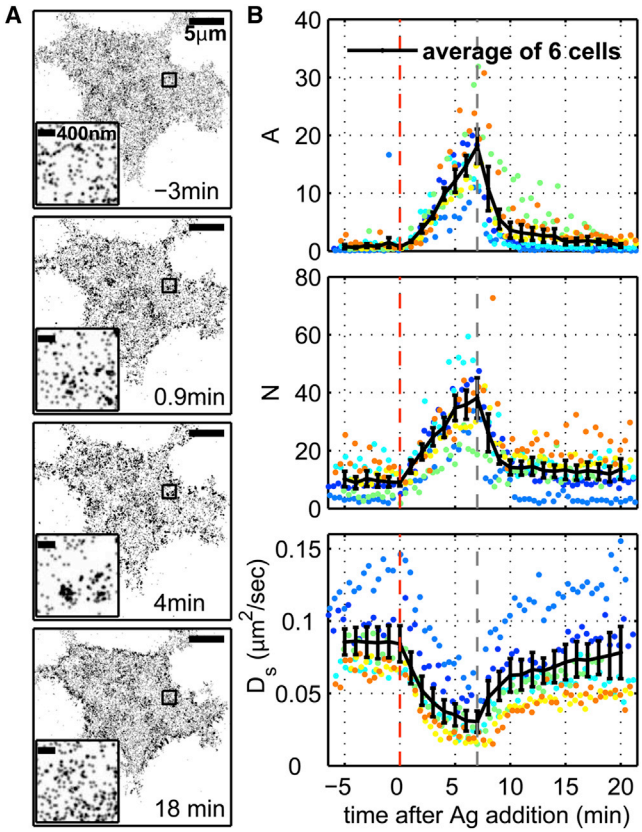

FIGURE 5 Antigen-induced changes in receptor clustering and mobility are reversible. (*A*) Reconstructed images of an AF647-IgE-labeled living cell before and after stimulation and subsequent addition of DCT. Each image is reconstructed from 80 s of acquired data. (*Insets*) Magnifications of the boxed regions in the main image. DNP-BSA (0.1 μg/ml) was added at 0 min, and DCT (200 μM) was added at 7 min. (*B*) The parameters A, N, and D_s are calculated as in Figs. 1 *C* and 2 *C*. The average values of A, N, and D_s, indicated by black lines, for six live-cell experiments distinguished by different colors, over the time course of stimulation and DCT addition. Antigen addition is indicated by the orange dashed line at 0 min, and DCT addition is indicated by the gray dashed line at 7 min. To see this figure in color, go online.

that the densely packed and immobile receptor clusters formed within 7 min of antigen addition are not stabilized solely through interactions with other cellular components or that these interactions are insufficient to stabilize clusters in the absence of antigen cross-linking.

Receptor organization and mobility in response to cholesterol perturbation in unstimulated cells

To examine the role of lipid-mediated membrane heterogeneity on early and later stages of antigen stimulation, we investigated the impact of membrane cholesterol levels on receptor organization and mobility. Receptor diffusion (D_S) and clustering (N) upon cross-linking with antigen are measured for multiple live cells exposed to either methyl-β-cyclodextrin (MβCD) to reduce plasma membrane cholesterol or MβCD precomplexed with cholesterol (MβCD + chol) to enrich plasma membrane cholesterol (Figs. 6 and S5). Under our conditions, we expect an ~20% decrease in the total cellular cholesterol content after 5 min of MβCD addition and an ~50% decrease after 15 min (48).

In the absence of cross-linking by antigen, local receptor density changes due to variations in membrane cholesterol concentration. Fig. S5 shows representative superresolution images of AF647-IgE/FcεRI with and without antigen treatment for individual cells with MβCD or MβCD + chol. IgE-FcεRI continues to show largely random distribution in unstimulated cells with reduced cholesterol levels, but becomes tightly clustered in unstimulated cells with elevated cholesterol levels. This visual observation is quantified in Fig. S6, where D_S, A, and N are plotted as a function of time and treatment with MβCD or MβCD + chol.

It is likely that other cellular processes contribute to the organization and mobility of receptors in cholesterol-loaded cells. For example, we observe robust antigen-independent activation of transient Ca^{2+} oscillations after cells are incubated with MβCD + chol for 2 min, and this persists until ~5 min after MβCD + chol is added (Figs. S7 and 6, *B* and *C*). This indicates that the cellular environment changes dramatically in response to MβCD + chol in ways that may not be directly related to cholesterol's effects on lipid-mediated membrane organization. Modulating cellular cholesterol levels also leads to changes in receptor diffusion in unstimulated cells. MβCD addition to unstimulated cells results in a time-dependent decline in D_S over 15 min, and incubation with MβCD + chol leads to slight increases in D_S (Fig. S6), despite the large increases in receptor clustering described above. These observations could be the result of changes in membrane surface area, changes in the surface density of immobile obstacles, or induction of solid-phase domains (49).

Receptor organization and mobility in response to cholesterol perturbation in stimulated cells

Perturbations of membrane cholesterol also affect the organization and mobility of IgE-FcεRI complexes when receptors are subsequently cross-linked with multivalent antigen (Fig. 6 *A*). For both cholesterol reduction and enrichment, receptor clustering increases and receptor diffusion decreases in response to antigen, qualitatively similar to trends in the absence of perturbation (Figs. 3 *A* and 6 *A*). We observe two distinct regimes in plots of D_S versus N for points after antigen addition in cells pretreated with MβCD, as is also observed in cells in the absence of cholesterol modulation. The crossover between these two regimes occurs at larger values of N in cells with reduced cholesterol levels ($N < 40$ for untreated versus $N > 60$ for MβCD-treated cells (Fig. 6 *A*, *upper*)), which also corresponds to longer stimulation times at the crossover point (~1 min for untreated vs. ~3 min for MβCD-treated cells).

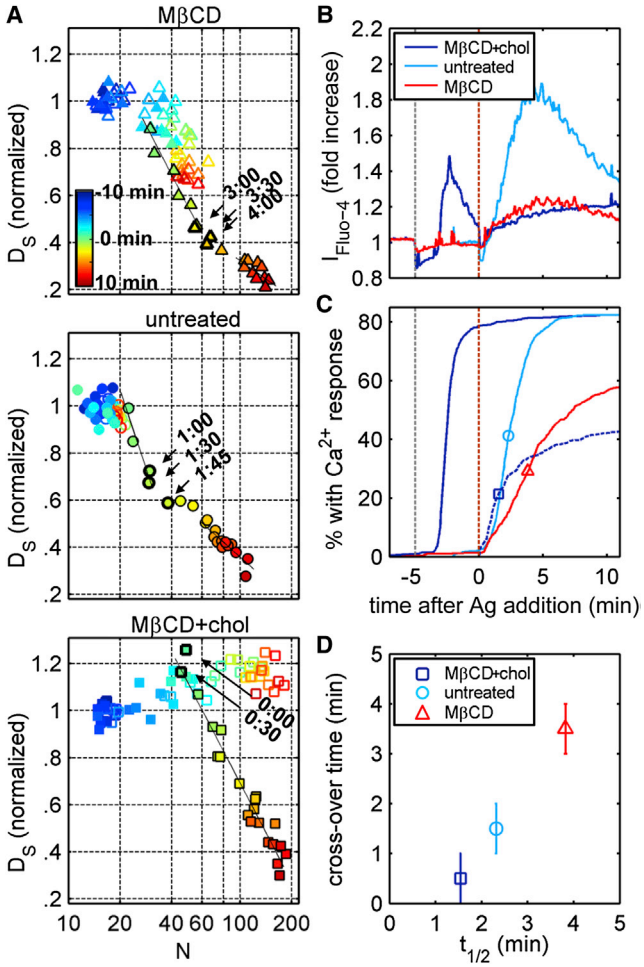

FIGURE 6 Perturbations of membrane cholesterol have corresponding effects on receptor diffusion, receptor clustering, and cellular Ca^{2+} responses. (*A*) Average D_S and N from five live cells for each of six treatments—MβCD (*upper*), no perturbation (*middle*), or MβCD + chol (*lower*)—in the presence (*solid symbols*) and absence (*open symbols*) of antigen stimulation (0.1 μg/ml). Changing color from blue to red indicates advancement in time by 30 s for each time point from −10 to 10 min after the addition of antigen for stimulated cells or a blank addition of buffer for unstimulated cells. Cholesterol perturbations are added, where applicable, at −5 min. For stimulated time points (*solid symbols outlined in black*), the fit lines shown in black represent linear fits of the time points belonging to the two regimes of D_S dependence on N, weighted by the inverse of the the mean ± SE in D_S and N. Stimulated time points near the crossover are indicated by arrows and labeled with time after antigen addition. (*B*) Total fluorescence intensity is shown as a function of time for populations of cells (at least 500) loaded with Fluo-4-AM and treated with MβCD, MβCD + chol, or no perturbation. The dotted gray line at −5 min indicates the addition of MβCD or MβCD + chol, and the dotted orange line indicates the addition of antigen. (*C*) The cumulative distribution in time of cells with an initial Ca^{2+} response as monitored by Fluo-4 fluorescence. The dark blue dotted line indicates the cumulative distribution of cells treated with MβCD + chol that exhibit an additional Ca^{2+} response after the addition of antigen. The half-maximum times ($t_{1/2}$) of cumulative curves are denoted by open symbols. (*D*) The estimated midpoints of the crossover times are plotted versus $t_{1/2}$ for each cholesterol treatment. Error bars represent uncertainty in determining the midpoint of the crossover time by ±30 s.

For cells pretreated with MβCD + chol (Fig. 6 *A*, *lower*), only one regime is apparent in plots of D_S versus N, and the N is larger before antigen addition.

Antigen-induced functional responses are also affected in cells pretreated with MβCD or MβCD + chol. Antigen-induced signaling is less effective in cells with reduced cholesterol levels when stimulated degranulation is assessed (50–53) (Fig. S8). When Ca^{2+} mobilization is again used as a rough measure of the onset of cellular signaling, as in Fig. 3, pretreatment of cells with MβCD results in a Ca^{2+} response that is both reduced in magnitude (Fig. 6 *B*) and delayed (Fig. 6 *C*) compared to untreated cells. A fraction (~40%) of cells pretreated with MβCD fail to show Ca^{2+} responses within 10 min after antigen addition. We quantify the timing of antigen-induced Ca^{2+} mobilization by measuring the time taken for 50% of responding cells to show an initial Ca^{2+} response, $t_{1/2}$, as indicated by the symbols on the cumulative distributions shown in Fig. 6 *C*. Antigen-induced signaling is attenuated in cells pretreated with MβCD + chol when they are assayed by degranulation (Fig. S8) or by measurement of Ca^{2+} mobilization (Fig. 6).

For the case of cholesterol enrichment, we observe an initial Ca^{2+}response after MβCD + chol is added, as described above, followed by a second, weaker Ca^{2+} signal in response to antigen (Fig. 6 *B*). A large fraction (~60%) of MβCD + chol-treated cells also fail to exhibit an antigen-induced Ca^{2+} response (Fig. 6 *C*), although cells that do respond do so with a minimal time lag after antigen addition. As a result, $t_{1/2}$ is shorter compared to either untreated or MβCD-treated cells (Fig. 6 *D*). These differences in the nature of the antigen-dependent Ca^{2+} response may be influenced by the MβCD + chol-induced Ca^{2+} transient observed before antigen addition. The shape, frequency, and duration of Ca^{2+} oscillations are also severely affected by changes in cellular cholesterol (Fig. S7).

$t_{1/2}$ is correlated with the timing of the crossover observed in plots of D_S versus N for the three cholesterol treatments (Fig. 6 *D*). Despite the uncertainty in relating the timing of Ca^{2+} mobilization to superresolution measurements discussed above, we observe differences in the relative timing of the crossover and $t_{1/2}$ that are both dependent on cholesterol perturbation. This observation supports our conclusion that the initial, rapid decrease in the diffusion coefficient of IgE-FcεRI receptors is a consequence of interactions that precede Ca^{2+} mobilization, whereas the accumulation of receptors into densely packed clusters represents receptors after the onset of signaling. For the case of cholesterol reduction, antigen-induced slowing of receptor diffusion occurs at a slower rate than in untreated or cholesterol-enriched cells (Fig. 6 *A*), suggesting that initial signaling steps occur over a longer time period. This is consistent with our observations of a slower Ca^{2+} response in MβCD-treated cells compared to untreated cells. The crossover between regimes occurs at larger values of N in MβCD treated versus untreated cells,

suggesting that more receptors are needed to initiate downstream signaling events when cholesterol levels are reduced. Plots of Ds versus N for cholesterol-enriched cells indicate only a single regime, and antigen-induced Ca^{2+} responses occur with a minimal time lag after antigen addition.

Previous work has demonstrated the importance of membrane-lipid-mediated protein targeting for transmembrane signaling in the FcεRI cascade (54,55). Cholesterol reduction inhibits stimulated receptor phosphorylation by Lyn, and productive signaling only occurs upon the redistribution of receptors, kinases, and phosphatases via changes in the local lipid environment surrounding cross-linked receptors (53,56,57). In our previous SEM work we found that cholesterol reduction before antigen addition led to smaller IgE-FcεRI-rich clusters and reduced Lyn partitioning into receptor-rich clusters when cells were chemically fixed 1 min after antigen addition at 37°C. Although it is not possible to compare absolute numbers between these experiments due to the different labeling strategies employed, our current findings are consistent with these previous results. Specifically, we find that it takes longer for receptors to assemble into tight clusters when cells are pretreated with MβCD, so at a given time point after stimulation, we would expect receptor-rich clusters to be smaller in MβCD-pretreated cells compared to untreated cells. Our observations of a delay in Ca^{2+} responses in MβCD-pretreated cells relative to untreated cells are consistent with our past observations of defects in Lyn recruitment under these conditions. These findings are consistent with an inhibitory role for cholesterol reduction in signaling that has been supported by previous observations (50,52,53). An alternative explanation for the changes in diffusion versus clustering behavior and Ca^{2+} responses observed in MβCD- and MβCD + chol-treated cells are related to more global effects of cholesterol modulation, such as its perturbation of the actin cytoskeleton. Cholesterol reduction can disrupt cytoskeleton-membrane attachment through perturbation of plasma membrane PIP_2 (58), or because actin is frequently coupled to the plasma membrane via more ordered regions (59). Therefore, the changes in receptor clustering, receptor mobility, and Ca^{2+} responses caused by MβCD, and by extension MβCD + chol, may be indirect results of membrane cholesterol modulation via its effects on the actin cytoskeleton.

CONCLUSION

In conclusion, we demonstrate that superresolution fluorescence localization imaging is a powerful method for quantifying the organization and mobility of immune receptors in cells undergoing stimulated responses. Simultaneous measurements of clustering and diffusion enable the resolution of two distinct temporal phases of receptor clustering and immobilization. At early times after stimulation, receptor-rich clusters increase marginally in size and receptors slow dramatically when averaged over the population of receptors. When examined as individual molecules, either as monomers or as members of clusters, single receptors appear to reversibly associate with small and slowly moving receptor clusters soon after the addition of antigen. These behaviors are observed at stimulation times preceding Ca^{2+} mobilization, leading us to conclude that they arise from interactions associated with initial signaling steps. At later times, receptors in clusters become increasingly dense and are largely immobile. Since these behaviors occur at times after the initial Ca^{2+} response, we hypothesize that receptor immobilization into densely packed clusters leads to subsequent cellular interactions related to downregulation of signaling. Before these terminating steps, dense receptor clusters are dispersed when the cross-linking antigen is displaced by a monovalent ligand. Receptor clustering and dynamics are also altered in cells with modulated cholesterol levels. Most notably, receptors cluster in cells with increased cholesterol levels even in the absence of antigen, and we observe changes in the duration of the initial phase of receptor clustering and immobilization in stimulated cells with modulated cholesterol levels. The onset of Ca^{2+} mobilization requires association of activated receptors with multiple proteins, and this signaling complex formation appears to occur before or during the crossover between the two regimes defined by our analysis. We observe differences in the timing of Ca^{2+} mobilization for cells with modulated cholesterol levels that correspond to changes in the timing of the initial phase of clustering. These findings are motivators for future work investigating the physical interactions that give rise to the observed changes in receptor organization and mobility, and how these translate into cellular functions.

SUPPORTING MATERIAL

Eight figures, one movie, References (60–62), Supporting Results and Supporting Materials and Methods are available at http://www.biophysj.org/biophysj/supplemental/S0006-3495(13)01126-0.

The authors thank Amit Singhai for assistance with experiments and for providing reagents, and Christopher V. Kelly, Matthew B. Stone, and Benjamin B. Machta for helpful discussions.

Research was supported through grants from the National Institutes of Health to S.L.V. (R00GM087810) and B.B. and D.H. (RO1 AI018306). S.A.S. acknowledges partial support from a National Institutes of Health Molecular Biophysics Training Grant (T32GM008267).

REFERENCES

1. Siraganian, R. P. 2003. Mast cell signal transduction from the high-affinity IgE receptor. *Curr. Opin. Immunol.* 15:639–646.

2. Blank, U., and J. Rivera. 2004. The ins and outs of IgE-dependent mast-cell exocytosis. *Trends Immunol.* 25:266–273.

3. Gilfillan, A. M., and J. Rivera. 2009. The tyrosine kinase network regulating mast cell activation. *Immunol. Rev.* 228:149–169.
4. Schlessinger, J., W. W. Webb, …, H. Metzger. 1976. Lateral motion and valence of Fc receptors on rat peritoneal mast cells. *Nature.* 264: 550–552.
5. Menon, A. K., D. A. Holowka, …, B. A. Baird. 1986. Cross-linking of receptor-bound IgE to aggregates larger than dimers leads to rapid immobilization. *J. Cell Biol.* 102:541–550.
6. Stump, R. F., J. R. Pfeiffer, …, J. M. Oliver. 1988. Mapping gold-labeled IgE receptors on mast cells by scanning electron microscopy: receptor distributions revealed by silver enhancement, backscattered electron imaging, and digital image analysis. *J. Histochem. Cytochem.* 36:493–502.
7. Wilson, B. S., J. R. Pfeiffer, and J. M. Oliver. 2000. Observing FcεRI signaling from the inside of the mast cell membrane. *J. Cell Biol.* 149:1131–1142.
8. Veatch, S. L., E. N. Chiang, …, B. A. Baird. 2012. Quantitative nanoscale analysis of IgE-FcεRI clustering and coupling to early signaling proteins. *J. Phys. Chem. B.* 116:6923–6935.
9. Menon, A. K., D. A. Holowka, …, B. A. Baird. 1986. Clustering, mobility, and triggering activity of small oligomers of immunoglobulin E on rat basophilic leukemia cells. *J. Cell Biol.* 102:534–540.
10. Feder, T. J., I. Brust-Mascher, …, W. W. Webb. 1996. Constrained diffusion or immobile fraction on cell surfaces: a new interpretation. *Biophys. J.* 70:2767–2773.
11. Larson, D. R., J. A. Gosse, …, W. W. Webb. 2005. Temporally resolved interactions between antigen-stimulated IgE receptors and Lyn kinase on living cells. *J. Cell Biol.* 171:527–536.
12. Andrews, N. L., K. A. Lidke, …, D. S. Lidke. 2008. Actin restricts FcepsilonRI diffusion and facilitates antigen-induced receptor immobilization. *Nat. Cell Biol.* 10:955–963.
13. Andrews, N. L., J. R. Pfeiffer, …, D. S. Lidke. 2009. Small, mobile FcεRI receptor aggregates are signaling competent. *Immunity.* 31:469–479.
14. Spendier, K., K. A. Lidke, …, J. L. Thomas. 2012. Single-particle tracking of immunoglobulin E receptors (FcεRI) in micron-sized clusters and receptor patches. *FEBS Lett.* 586:416–421.
15. Rust, M. J., M. Bates, and X. Zhuang. 2006. Stochastic optical reconstruction microscopy (STORM) provides sub-diffraction-limit image resolution. *Nat. Methods.* 3:793–795.
16. Heilemann, M., S. van de Linde, …, M. Sauer. 2008. Subdiffraction-resolution fluorescence imaging with conventional fluorescent probes. *Angew. Chem. Int. Ed. Engl.* 47:6172–6176.
17. Betzig, E., G. H. Patterson, …, H. F. Hess. 2006. Imaging intracellular fluorescent proteins at nanometer resolution. *Science.* 313:1642–1645.
18. Hess, S. T., T. P. K. Girirajan, and M. D. Mason. 2006. Ultra-high resolution imaging by fluorescence photoactivation localization microscopy. *Biophys. J.* 91:4258–4272.
19. Greenfield, D., A. L. McEvoy, …, J. Liphardt. 2009. Self-organization of the *Escherichia coli* chemotaxis network imaged with super-resolution light microscopy. *PLoS Biol.* 7:e1000137.
20. Lillemeier, B. F., M. A. Mörtelmaier, …, M. M. Davis. 2010. TCR and Lat are expressed on separate protein islands on T cell membranes and concatenate during activation. *Nat. Immunol.* 11:90–96.
21. Owen, D. M., C. Rentero, …, K. Gaus. 2010. PALM imaging and cluster analysis of protein heterogeneity at the cell surface. *J. Biophotonics.* 3:446–454.
22. Williamson, D. J., D. M. Owen, …, K. Gaus. 2011. Pre-existing clusters of the adaptor Lat do not participate in early T cell signaling events. *Nat. Immunol.* 12:655–662.
23. Hsu, C.-J., and T. Baumgart. 2011. Spatial association of signaling proteins and F-actin effects on cluster assembly analyzed via photoactivation localization microscopy in T cells. *PLoS ONE.* 6:e23586.
24. Sherman, E., V. Barr, …, L. E. Samelson. 2011. Functional nanoscale organization of signaling molecules downstream of the T cell antigen receptor. *Immunity.* 35:705–720.
25. Gunewardene, M. S., F. V. Subach, …, S. T. Hess. 2011. Superresolution imaging of multiple fluorescent proteins with highly overlapping emission spectra in living cells. *Biophys. J.* 101:1522–1528.
26. Jones, S. A., S.-H. Shim, …, X. Zhuang. 2011. Fast, three-dimensional super-resolution imaging of live cells. *Nat. Methods.* 8:499–508.
27. Manley, S., J. M. Gillette, …, J. Lippincott-Schwartz. 2008. High-density mapping of single-molecule trajectories with photoactivated localization microscopy. *Nat. Methods.* 5:155–157.
28. Manley, S., J. M. Gillette, and J. Lippincott-Schwartz. 2010. Single-particle tracking photoactivated localization microscopy for mapping single-molecule dynamics. *Methods Enzymol.* 475:109–120.
29. Giannone, G., E. Hosy, …, L. Cognet. 2010. Dynamic superresolution imaging of endogenous proteins on living cells at ultra-high density. *Biophys. J.* 99:1303–1310.
30. Gadi, D., A. Wagenknecht-Wiesner, …, B. Baird. 2011. Sequestration of phosphoinositides by mutated MARCKS effector domain inhibits stimulated Ca^{2+} mobilization and degranulation in mast cells. *Mol. Biol. Cell.* 22:4908–4917.
31. Veatch, S. L., B. B. Machta, …, B. A. Baird. 2012. Correlation functions quantify super-resolution images and estimate apparent clustering due to over-counting. *PLoS ONE.* 7:e31457.
32. Erickson, J., B. Goldstein, …, B. Baird. 1987. The effect of receptor density on the forward rate constant for binding of ligands to cell surface receptors. *Biophys. J.* 52:657–662.
33. Barisas, B. G., S. M. Smith, …, D. A. Roess. 2007. Compartmentalization of the Type I Fc ε receptor and MAFA on mast cell membranes. *Biophys. Chem.* 126:209–217.
34. Xu, K., B. Goldstein, …, B. Baird. 1998. Kinetics of multivalent antigen DNP-BSA binding to IgE-Fc ε RI in relationship to the stimulated tyrosine phosphorylation of Fc ε RI. *J. Immunol.* 160:3225–3235.
35. Paolini, R., M. H. Jouvin, and J. P. Kinet. 1991. Phosphorylation and dephosphorylation of the high-affinity receptor for immunoglobulin E immediately after receptor engagement and disengagement. *Nature.* 353:855–858.
36. Ritchie, K., R. Iino, …, A. Kusumi. 2003. The fence and picket structure of the plasma membrane of live cells as revealed by single molecule techniques (Review). *Mol. Membr. Biol.* 20:13–18 (Review).
37. Murase, K., T. Fujiwara, …, A. Kusumi. 2004. Ultrafine membrane compartments for molecular diffusion as revealed by single molecule techniques. *Biophys. J.* 86:4075–4093.
38. Machta, B. B., S. Papanikolaou, …, S. L. Veatch. 2011. Minimal model of plasma membrane heterogeneity requires coupling cortical actin to criticality. *Biophys. J.* 100:1668–1677.
39. Pierini, L., N. T. Harris, …, B. Baird. 1997. Evidence supporting a role for microfilaments in regulating the coupling between poorly dissociable IgE-Fc εRI aggregates downstream signaling pathways. *Biochemistry.* 36:7447–7456.
40. Ra, C., K. Furuichi, …, K. N. White. 1989. Internalization of IgE receptors on rat basophilic leukemic cells by phorbol ester. Comparison with endocytosis induced by receptor aggregation. *Eur. J. Immunol.* 19:1771–1777.
41. Liu, C., H. Miller, …, W. Song. 2011. A balance of Bruton's tyrosine kinase and SHIP activation regulates B cell receptor cluster formation by controlling actin remodeling. *J. Immunol.* 187:230–239.
42. Lee, K.-H., A. R. Dinner, …, A. S. Shaw. 2003. The immunological synapse balances T cell receptor signaling and degradation. *Science.* 302:1218–1222.
43. Varma, R., G. Campi, …, M. L. Dustin. 2006. T cell receptor-proximal signals are sustained in peripheral microclusters and terminated in the central supramolecular activation cluster. *Immunity.* 25:117–127.
44. Weetall, M., D. Holowka, and B. Baird. 1993. Heterologous desensitization of the high affinity receptor for IgE (Fc ε R1) on RBL cells. *J. Immunol.* 150:4072–4083.
45. Saxton, M. J. 1997. Single-particle tracking: the distribution of diffusion coefficients. *Biophys. J.* 72:1744–1753.

46. Fewtrell, C. 1985. Calcium in Biological Systems. Plenum Press, New York.

47. Seagrave, J. C., G. G. Deanin, …, J. M. Oliver. 1987. DNP-phycobiliproteins, fluorescent antigens to study dynamic properties of antigen-IgE-receptor complexes on RBL-2H3 rat mast cells. *Cytometry.* 8:287–295.

48. Surviladze, Z., L. Dráberová, …, P. Dráber. 2001. Differential sensitivity to acute cholesterol lowering of activation mediated via the high-affinity IgE receptor and Thy-1 glycoprotein. *Eur. J. Immunol.* 31:1–10.

49. Nishimura, S. Y., M. Vrljic, …, W. E. Moerner. 2006. Cholesterol depletion induces solid-like regions in the plasma membrane. *Biophys. J.* 90:927–938.

50. Kato, N., M. Nakanishi, and N. Hirashima. 2003. Cholesterol depletion inhibits store-operated calcium currents and exocytotic membrane fusion in RBL-2H3 cells. *Biochemistry.* 42:11808–11814.

51. Yamashita, T., T. Yamaguchi, …, S. Nagasawa. 2001. Detergent-resistant membrane domains are required for mast cell activation but dispensable for tyrosine phosphorylation upon aggregation of the high affinity receptor for IgE. *J. Biochem.* 129:861–868.

52. Silveira e Souza, A. M. M., V. M. Mazucato, …, C. Oliver. 2008. The α-galactosyl derivatives of ganglioside GD(1b) are essential for the organization of lipid rafts in RBL-2H3 mast cells. *Exp. Cell Res.* 314:2515–2528.

53. Sheets, E. D., D. Holowka, and B. Baird. 1999. Critical role for cholesterol in Lyn-mediated tyrosine phosphorylation of FcεRI and their association with detergent-resistant membranes. *J. Cell Biol.* 145: 877–887.

54. Silveira E Souza, A. M. M., V. M. Mazucato, …, C. Oliver. 2011. Lipid rafts in mast cell biology. *J. Lipids.* 2011:752906.

55. Holowka, D., J. A. Gosse, A. T. Hammond, X. Han, P. Sengupta…, 2005. Lipid segregation and IgE receptor signaling: a decade of progress. *Biochim. Biophys. Acta.* 1746:252–259.

56. Field, K. A., D. Holowka, and B. Baird. 1997. Compartmentalized activation of the high affinity immunoglobulin E receptor within membrane domains. *J. Biol. Chem.* 272:4276–4280.

57. Young, R. M., D. Holowka, and B. Baird. 2003. A lipid raft environment enhances Lyn kinase activity by protecting the active site tyrosine from dephosphorylation. *J. Biol. Chem.* 278:20746–20752.

58. Kwik, J., S. Boyle, …, M. Edidin. 2003. Membrane cholesterol, lateral mobility, and the phosphatidylinositol 4,5-bisphosphate-dependent organization of cell actin. *Proc. Natl. Acad. Sci. USA.* 100:13964–13969.

59. Holowka, D., E. D. Sheets, and B. Baird. 2000. Interactions between FcεRI and lipid raft components are regulated by the actin cytoskeleton. *J. Cell Sci.* 113:1009–1019.

60. Naal, R. M. Z. G., J. Tabb, …, B. Baird. 2004. In situ measurement of degranulation as a biosensor based on RBL-2H3 mast cells. *Biosens. Bioelectron.* 20:791–796.

61. Hardy, R. R. 1986. Handbook of Experimental Immunology, 4th ed. Blackwell Scientific, Oxford, United Kingdom.

62. Jaqaman, K., D. Loerke, …, G. Danuser. 2008. Robust single-particle tracking in live-cell time-lapse sequences. *Nat. Methods.* 5:695–702.

Distinct Stages of Stimulated FcεRI Receptor Clustering and Immobilization Are Identified through Superresolution Imaging

Sarah A. Shelby,[†] David Holowka,[†] Barbara Baird,[†] and Sarah L. Veatch[‡]*

[†]Department of Chemistry and Chemical Biology, and Field of Biophysics, Cornell University, Ithaca, New York; and [‡]Department of Biophysics, University of Michigan, Ann Arbor, Michigan

SUPPORTING MATERIALS

SUPPORTING RESULTS

Live RBL-2H3 cells retain antigen-stimulated degranulation and Ca^{2+} responses under super-resolution imaging conditions.

To determine whether the buffer conditions required for dSTORM imaging affect the functional responses which result from IgE receptor cross-linking, a β-hexosaminidase release assay was used to measure the levels of secretory granule release in adherent RBL-2H3 cells in response to antigen stimulation conditions similar to those used in our live cell super-resolution experiments. This assay utilizes a fluorogenic substrate for the enzyme β-hexosaminidase, a constituent of secretory granules, to measure its release as a consequence of degranulation and quantify the extent of degranulation in RBL-2H3 cells (1). Control samples were stimulated under conditions that are conducive to degranulation in balanced salt solution with 1 mg/ml BSA (BSS-BSA, 30mM HEPES, 135mM NaCl, 5mM KCl, 1mM $MgCl_2$, 1.8mM $CaCl_2$, 5mM glucose, and 1mg/ml BSA at pH 7.4) at 37°C. Our super-resolution imaging buffer is buffered with Tris and has a higher pH than BSS (pH 8), contains the reducing agents and oxygen scavenging enzymes necessary for dSTORM imaging of AlexaFluor 647, and also has a higher concentration of glucose (55mM), which is a substrate for the oxygen-scavenging enzyme glucose oxidase. To determine the effects of the various components of the imaging buffer on cellular degranulation, cells were stimulated in imaging buffer with or without 50mM of glutathione (GTT) and oxygen scavenging enzymes. These cells degranulate to a slightly lesser extent than cells stimulated in BSS-BSA (Fig. S1 *A*), although degranulation is still robust. Degranulation in the presence of this buffer is reduced to levels between 75 and 90% of degranulation measured in BSS-BSA according to data shown in Fig. S1 and Fig. S8. Cellular degranulation measured in cells in imaging buffer without a reducing agent or oxygen scavenging enzymes is not significantly different from degranulation of cells in imaging buffer that contains both 50mM glutathione and oxygen scavenging enzymes. The decreased degranulation of cells in imaging buffer that contains both 50mM glutathione and oxygen scavenging enzymes compared to cells in BSS-BSA appears to be due to other components of the imaging buffer that differ from BSS-BSA, possibly the increased glucose concentration, Tris buffer, or increased pH. Stimulated cellular degranulation is substantially less when a higher concentration of glutathione is used or when β-mercaptoethanol is used as the imaging buffer reducing agent. For this reason a 50mM glutathione was chosen to minimize the impact of imaging buffer conditions on cellular responses, and the final formulation of the imaging buffer (IB) contains 30mM Tris, 135mM NaCl, 5mM KCl, 1mM $MgCl_2$, 1.8mM $CaCl_2$, 55mM glucose, 500μg/mL glucose-oxidase, 40μg/mL catalase, and 50mM glutathione at pH 8.

The effect of imaging buffer on Ca^{2+} mobilization was assessed through imaging experiments where sensitized RBL-2H3 cells are loaded with the Ca^{2+}-sensitive dye Fluo-4 and stimulated with multivalent antigen (DNP-BSA) in the presence of imaging buffer at room temperature (Fig. S1, *A* and *B*). Fluorescence intensity is monitored across a field of several hundred cells as a function of stimulation time, as described in Materials and Methods. Cells produce a robust Ca^{2+} response in the presence of imaging buffer after stimulation by antigen compared to cells imaged and stimulated in the conventional live cell imaging buffer, BSS-BSA (Fig. S1 *B*). The cumulative distribution of cells with an initial Ca^{2+}response indicates that the onset of Ca^{2+} mobilization in the population of cells is not substantially delayed or otherwise affected by imaging buffer (Fig. S1 *C*).

Redistribution of IgE-FcεRI after antigen addition as imaged in chemically fixed cells.

Super-resolution fluorescence localization imaging of IgE-FcεRI at the ventral (bottom) surface of chemically fixed RBL-2H3 cells reveals time-dependent receptor clustering due to cross-linking by antigen (Fig. S2), in good agreement with previous electron microscopy studies (2). Cells were sensitized by incubating with IgE antibodies specific for DNP, stimulated with the multivalent antigen DNP-BSA, and then chemically fixed at specified time points after antigen addition, as described in Materials and Methods. IgE-FcεRI complexes were fluorescently labeled either by sensitizing with IgE directly conjugated to Alexa Fluor 647 (AF647) (Fig. S2 *A* and *B*), or by sensitizing cells with two distinct pools of IgE directly conjugated either to AF647 or to Alexa Fluor 532 (AF532) prior to antigen addition and fixation (Fig. S2 *C*). Conventional TIRF images of the single-color fixed cells (Fig. S2 *A*) were captured before single-color super-resolution images (Fig. S2 *B*) and are shown for comparison. For super-resolution images with both single- and two-color labeling, IgE-FcεRI appears weakly structured in unstimulated cells (-Ag) and exhibits a clustered appearance in cells after stimulation (+Ag). One minute after antigen addition, labeled IgE-FcεRI-rich patches become apparent around the periphery of the cell's ventral surface, likely because this is the area accessed first by antigen. After incubation with antigen for 5 or 10 min, cells contain distinct IgE-FcεRI puncta on the ventral cell surface. Conventional TIRF imaging also shows large-scale receptor organization, including receptor puncta in stimulated cells, but structures under ~250nm cannot be resolved.

As with live cell experiments, we utilize spatial pair correlation functions to quantify clustering of IgE-FcεRI complexes in single-color reconstructed images of fixed cells. In single color experiments, multiple AF647 fluorophores can label each IgE antibody and each AF647 fluorophore can reversibly transition between fluorescent and non-fluorescent states within a single experiment. These phenomena result in apparent clustering on the size-scale of the localization precision in super-resolution images, such as those shown in Fig. S2 *B*, and corresponding artifacts in the quantification of images due to over-counting of single receptors (3). Pair cross-correlation functions are not subject to over-counting artifacts(3), are tabulated from two-color images, and measure the normalized probability of finding a localized fluorophore of one color a given distance, r, away from the average localized fluorophore of the second color. Average cross-correlation functions tabulated from unstimulated and stimulated cells are shown in Fig. S2 *D*.

Measured cross-correlation functions are fit to a single filtered exponential to extract information on average cluster size and density (3):

$$g_{Fit}(r) = g_{PSF}(r)*[1+ (Aexp(-r/\xi))]. \quad (S\ 1)$$

A is the amplitude of correlations, which is related to the increased density of receptors in clusters, ξ is the correlation length, which is approximately the average cluster radius, and $g_{PSF}(r)$ is a function that applies a Gaussian filter with width proportional to the resolution of the image. Measured cross-correlation functions were fit for all radii r<500nm. Details of the fitting methods and the determination of the resolution of the image are described in Materials and Methods. Simulated receptor density distributions which are reconstructed from our observed cross-correlation functions are shown in the right panels of Fig. S2 *D* and serve as a visual aid to represent receptor distributions in the absence of over-counting. We also fit autocorrelation functions tabulated from single color images to Eqn. S1 after first subtracting expected contributions from over-counting, assuming an average surface density of IgE-FcεRI complexes of 200/μm^2 (3, 4). Summaries of extracted values for ξ and A from both single and two color images are shown in Fig. S2 *E* and F along with our past results applying a similar analytical

methodology to scanning electron microscopy (SEM) images of IgE-FcεRI on the dorsal surface of RBL-2H3 cells labeled post fixation with primary and gold-conjugated secondary antibodies (2).

In unstimulated cells (-Ag), the cross-correlation of AF647 and AF532 probes is close to one at all radii, indicating that IgE-FcεRI complexes are nearly randomly distributed on the membrane (Fig. S2 *D*). Upon closer inspection, cross-correlation functions tabulated from images of cells indicate the presence of weak, long-range correlations in cells in the absence of antigen (inset of Fig. S2 *D*). The size of correlations in unstimulated cells is comparable to the size of clusters at long stimulation times, but the amplitude associated with these correlations is only 20% greater than a random distribution of receptors (Fig. S2 *D* inset), and two orders of magnitude less than the correlation amplitude 5 min following antigen stimulation. The simulated receptor distribution displayed in Fig. S2 *D* (lowest right panel) that corresponds to the unstimulated correlation function is a visual representation of these weak correlations and is nearly indistinguishable from a random distribution. We previously proposed that weak, long-range, unstimulated clustering may arise from non-planar topology of the ventral membrane, from weak lipid-mediated organization in unstimulated cells (3), or through direct or indirect coupling to cortical actin (5, 6). We note that no equivalent correlations were observed in our previous SEM work in unstimulated cells, which selected for flat regions of the dorsal cell surface (2). Also, weak correlations are dominated by over-counting artifacts in autocorrelation functions tabulated from unstimulated cells labeled with a single color. Errors in the estimation of correlations from over-counting likely result in an underestimation of ξ and an over-estimation of A for single-color measurements.

Cross-correlation functions become larger than one at short radii in cells incubated with multivalent antigen prior to fixation, indicating that receptors become clustered. With increasing stimulation time, cross-correlations increase in magnitude at short radii. Cross-correlation functions, calculated from images of stimulated cells, remain larger than one out to radii of 200 nm, indicating that the largest clusters have approximately this radius. This quantitative treatment is consistent with the qualitative observation of clustering in representative images shown in Fig. S2, *B* and *C*. Variations in the size (ξ) and magnitude (A) of correlations as a function of stimulation time provide a quantitative measure of receptor redistribution with cross-linking. We observe a slight increase in the size of cross-linked receptor clusters (ξ) within 5 min after stimulation, similar to the modest increase we observe in live cells after stimulation (Fig. 1C).Values of ξ are in relatively good agreement with our past SEM data, which, like our single-color experiments, are corrected for over-counting (Fig. S2 *E*) (2). Observed differences between the dorsal cell surface imaged by SEM and the ventral cell surface imaged by super-resolution microscopy, could arise from different accessibility to antigen or differences arising from adhesion to the substrate.

The amplitude of correlations (A) also increases with stimulation time, corresponding to an increase in receptor density in clusters (Fig. S2 *F*). It is notable that the correlation amplitude is substantially larger in stimulated cells in super-resolution measurements when compared to our previous SEM studies (Fig. S2 *F*). This indicates that clustered fluorescent labels in these optical microscopy measurements are more densely packed than the gold particles observed by SEM. This could be accounted for if gold particles are precluded from labeling some IgE-FcεRI complexes in densely packed receptor clusters due to the large relative size of the primary and secondary antibodies and gold particles (10 nm diameter). Values of ξ and A extracted from single color and two color images are in good general agreement aside from systematic reductions in ξ and elevation in A for single-color data.

Again, these systematic errors are expected with underestimation of correlations due to over-counting in the single color measurements, since remaining contributions from over-counting would act to decrease ξ and increase A.

Cholesterol perturbations affect antigen-stimulated degranulation and Ca^{2+} responses in live cells.

To probe the effects of cholesterol perturbations on signaling downstream of initial receptor clustering, we observed the Ca^{2+} responses of cells subjected to cholesterol depletion using methyl-beta-cyclodextrin (MβCD) or cholesterol enrichment using MβCD -cholesterol (MβCD+chol) similar to conditions used for live cell super-resolution experiments. Cytoplasmic Ca^{2+} concentrations were imaged using the Ca^{2+}-sensitive dye Fluo-4 for large fields of cells treated with MβCD or MβCD+chol (or neither in the case of control cells) followed by stimulation with antigen as described in the Materials and Methods and shown in Fig. 6. We observe perturbation-dependent differences in the shape, duration, and frequency of oscillations in the Fluo-4 intensity traces for individual cells (Fig. S7). Compared to untreated cells, Ca^{2+} oscillations due to the addition of antigen are delayed in individual MβCD-treated cells, and oscillations are less frequent (Fig.S7, top), consistent with the attenuated total intensity and delayed onset of initial Ca^{2+} responses we observe for the population of cells (Fig. 6, *B* and *C*). MβCD+chol treated cells begin to display Ca^{2+} oscillations upon the addition of MβCD+chol. These oscillations are robust for ~2 min but decrease in amplitude quickly after that time. Upon antigen addition, MβCD+chol-treated cells exhibit solitary, low-amplitude increases in cytoplasmic Ca^{2+} but do not display regular oscillations as in the case of untreated cells.

The β-hexosaminidase release assay was used to measure the levels of degranulation in adherent RBL-2H3 cells in response to cholesterol perturbation and antigen stimulation conditions similar to those used in our live cell cholesterol perturbation super-resolution experiments (Fig. 6). Cholesterol reduction results in a slight increase in spontaneous degranulation in the absence of antigen and a decrease in antigen-stimulated degranulation compared to cells in the presence or absence of antigen which are not subjected to cholesterol perturbation (Fig. S8). Similar experiments have previously been reported in the literature and have shown mixed results for the effect of cholesterol reduction on degranulation, where some report enhanced degranulation without stimulation and/or inhibited degranulation in the presence of antigen, and others do not observe significant changes (7–11). However, these previous experiments were conducted under varying conditions of cholesterol reduction, stimulation, etc, which may have significant effects on degranulation measurements. Cholesterol enrichment strongly inhibits degranulation either in the presence or absence of antigen. This suggests that although we observe clustering in super-resolution experiments and transient increases in cytoplasmic Ca^{2+} upon treatment of cells with MβCD+chol, these responses to cholesterol loading do not result in signaling sufficient for degranulation.

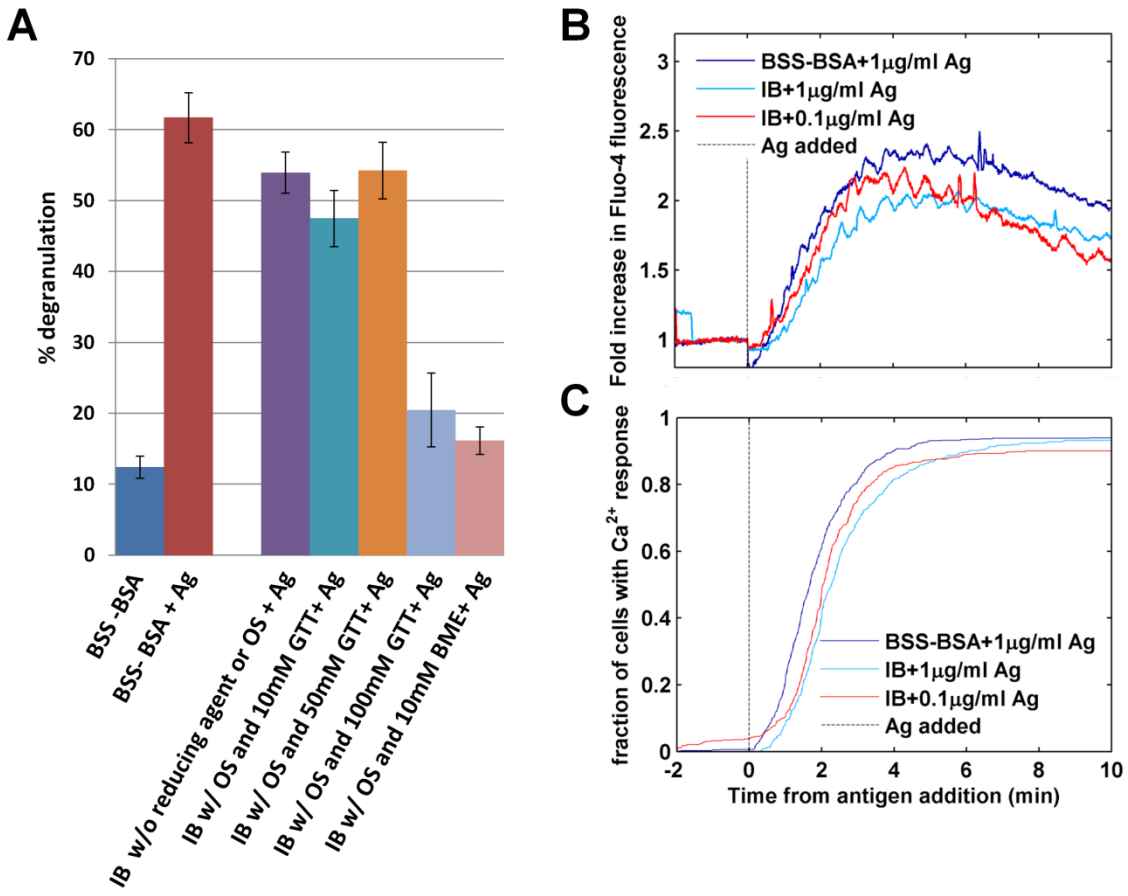

Fig. S1: RBL-2H3 cells retain the antigen-stimulated responses in super-resolution imaging buffer. (A) RBL-2H3 degranulation at 37°C was measured using a β-hexosaminidase release fluorogenic assay in which the effects of the oxygen scavenging enzymes (OS) and reducing agent used in the dSTORM imaging buffer (IB), including glutathione (GTT) or beta-mercaptoethanol (BME), were tested on antigen-stimulated degranulation. Cells in BSS-BSA in the presence or absence of DNP-BSA (1 μg/ml) were used as standards for basal and stimulated degranulation, respectively. (B) Antigen-stimulated Ca^{2+}mobilization was measured in the presence of imaging buffer at room temperature using Fluo-4 intensity as a readout of intracellular Ca^{2+} concentration. Total fluorescence intensity is shown for populations of cells (at least 500) loaded with Fluo-4-AM and stimulated with 1μg/ml or 0.1 μg/ml multivalent antigen (DNP_{24}-BSA) in BSS-BSA or in the presence of super-resolution imaging buffer as a function of time. The dotted gray line at 0 min indicates the addition of antigen. The signal is normalized to initial levels, and intensity is reported as a fold increase from initial levels. (C) Cumulative curves of Ca^{2+} mobilization initiation events of individual cells as a function of time. The number of cells which have initiated a Ca^{2+} response is plotted as the fraction of the total number of cells which displayed a Ca^{2+} response during the experiment.

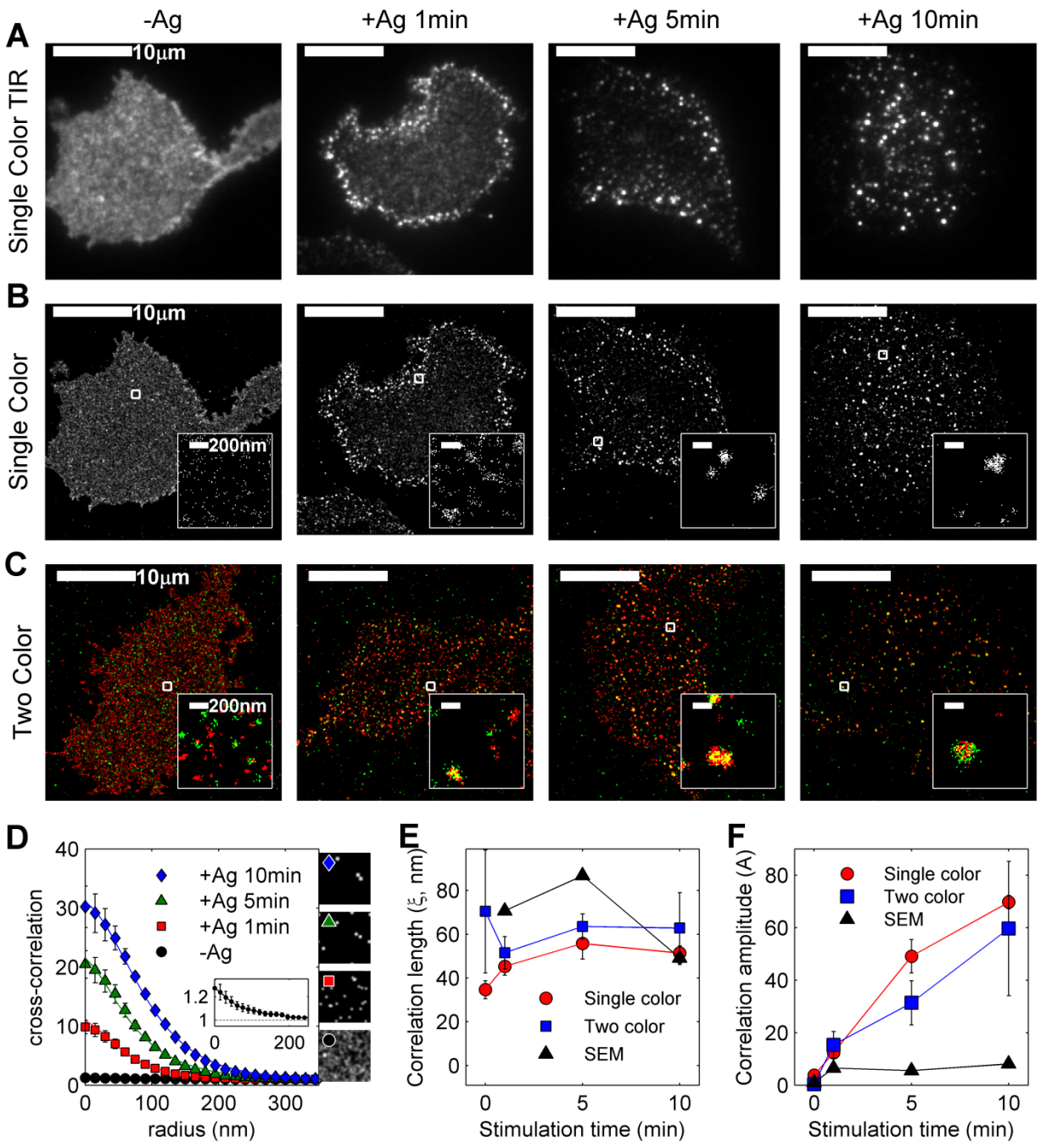

Fig. S2: Quantitative super-resolution localization microscopy TIRF imaging of IgE-FcεRI redistribution after antigen addition in chemically fixed cells. Representative TIRF images of RBL-2H3 cells imaged using either (A)conventional TIRF microscopy, (B) single-color, or (C) two-color super-resolution fluorescence localization microscopy in unstimulated cells and cells treated with the multivalent antigen DNP-BSA (1 μg/ml) at 37°C for the time indicated before chemical fixation. Conventional TIRF and single color super-resolution images are shown for the same 4 cells in (A) and (B), respectively, for purposes of comparison between super-resolution and conventional images. Single-color cells in (A) and

(B) are sensitized with IgE directly conjugated to AF647, while two-color measurements in (C) were conducted on cells sensitized with IgE directly conjugated to either AF647 (red) or AF532 (green) fluorophores. (D) Cross-correlation curves evaluated from two-color measurements averaged over at least 5 cells for each stimulation condition shown in (C). Error bars represent the standard error of the mean of values between cells. Lines are a fit to Eqn. S1 for radii between 0 and 500nm. Simulated receptor distributions over a 2μm by 2μm area which recapitulate observed correlation functions for each time point are shown at right. Extracted correlation lengths (E) and amplitudes (F) from super-resolution fluorescence localization imaging measurements are compared to previous scanning electron microscopy (SEM) measurements (2). Values reported for two-color measurements represent the average over multiple cells with error bounds denoting the standard error of the mean. For single-color measurements, values are obtained by correcting measured correlation functions for over-counting assuming a receptor density of 200/μm^2, and fitting the resulting curve to Eqn. S1 for radii between 40 and 300nm.

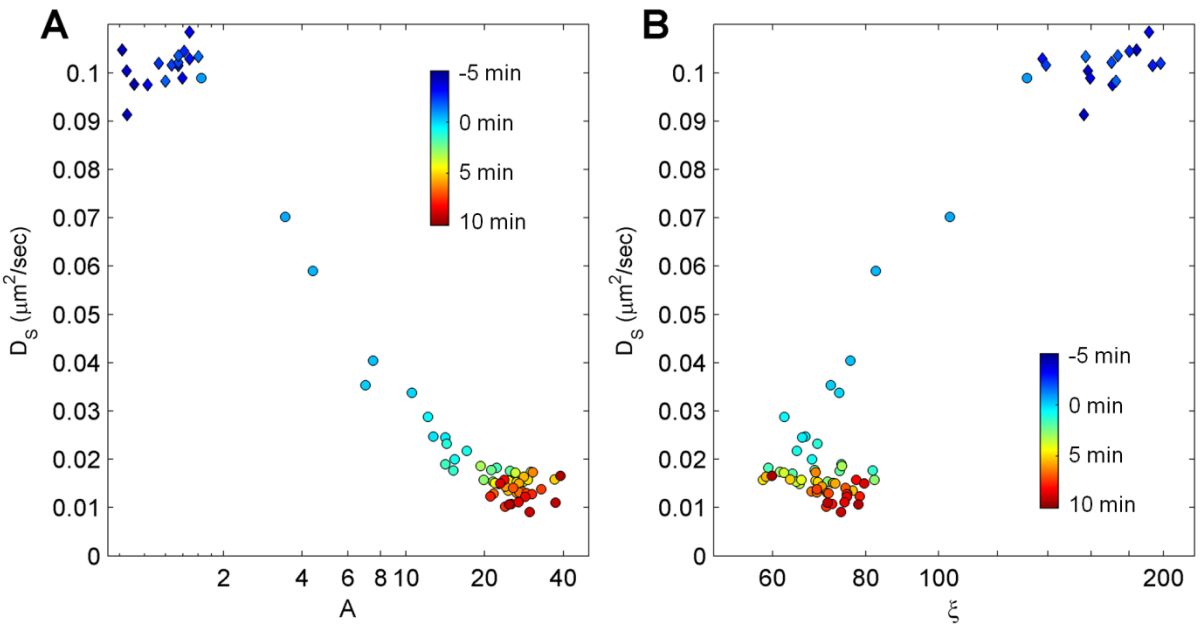

Fig. S3: Average receptor diffusion vs. correlation amplitude and correlation length. Average short time diffusion coefficient (as in Fig. 2 *C*) is shown as a function of the correlation function parameters, the correlation amplitude A (A) and the correlation length ξ (B) (as in Fig. 1 *C*). Each point corresponds to values of D_s and A or ξ at a given time before (diamonds) and after (circles) stimulation averaged over the 11 cells imaged, and data from individual cells are binned every 15 s to facilitate averaging. These plots are related to Fig. 3 A because the parameters N, A, and ξ are not independent. If correlation functions are well approximated by exponentials, then $N \approx 2A\xi^2\rho$, where ρ is the average receptor density which is assumed to be 200/μm^2 (4). In Fig. 3 A, N is determined without fitting according to Eqn. 2. Time after the addition of antigen is indicated by the color bar. Antigen (1 μg/ml) is added at time = 0, after the cells were imaged for 5 min.

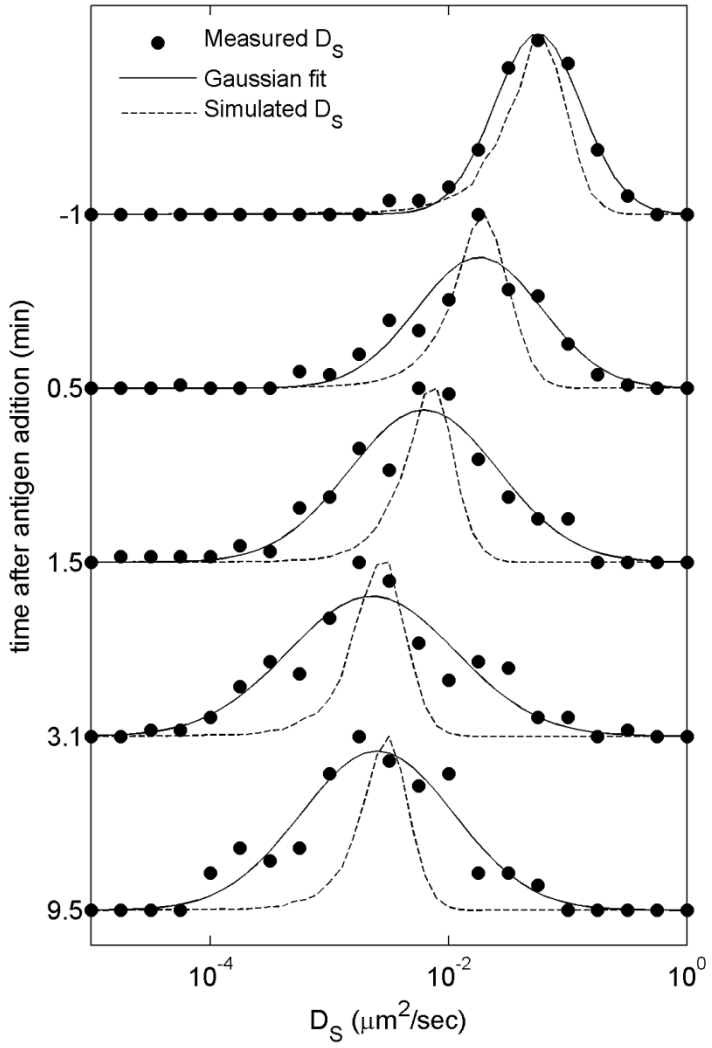

Fig. S4: Distributions of single-trajectory diffusion constant are broader than expected for Brownian diffusion post-stimulation. Histograms showing the distribution of single molecule diffusion coefficients (D_S) are repeated from Fig. 4 *B* (solid points) and compared with histograms generated by extracting D_S from simulated Brownian trajectories with the same distribution of track lengths observed in experiments (dashed lines). The width and asymmetric shape of simulated histogram arises from their being finite track lengths (at least 16 segments). Before the addition of antigen (top), the widths of diffusion coefficient histograms are well approximated by the Brownian simulation, suggesting a homogenous population of receptors is resolved in these measurements. After stimulation, measured histograms shift to lower values of D_S, and broaden when compared to the Brownian simulations.

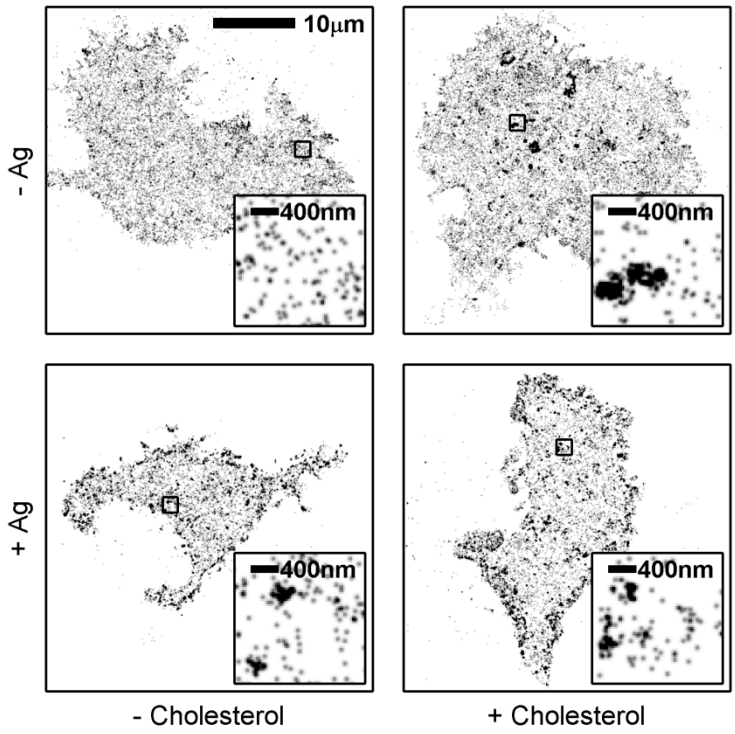

Fig. S5: Perturbations of membrane cholesterol alter receptor clustering. Representative images of live cells after 15 min of 10mM MβCD (left) or MβCD+chol(right) in the absence (top) or presence (bottom) of incubation with 0.1 μg/ml antigen for 10 min. Images are reconstructed from 80 s of acquired data. Insets show magnified images of the regions outlined with black squares.

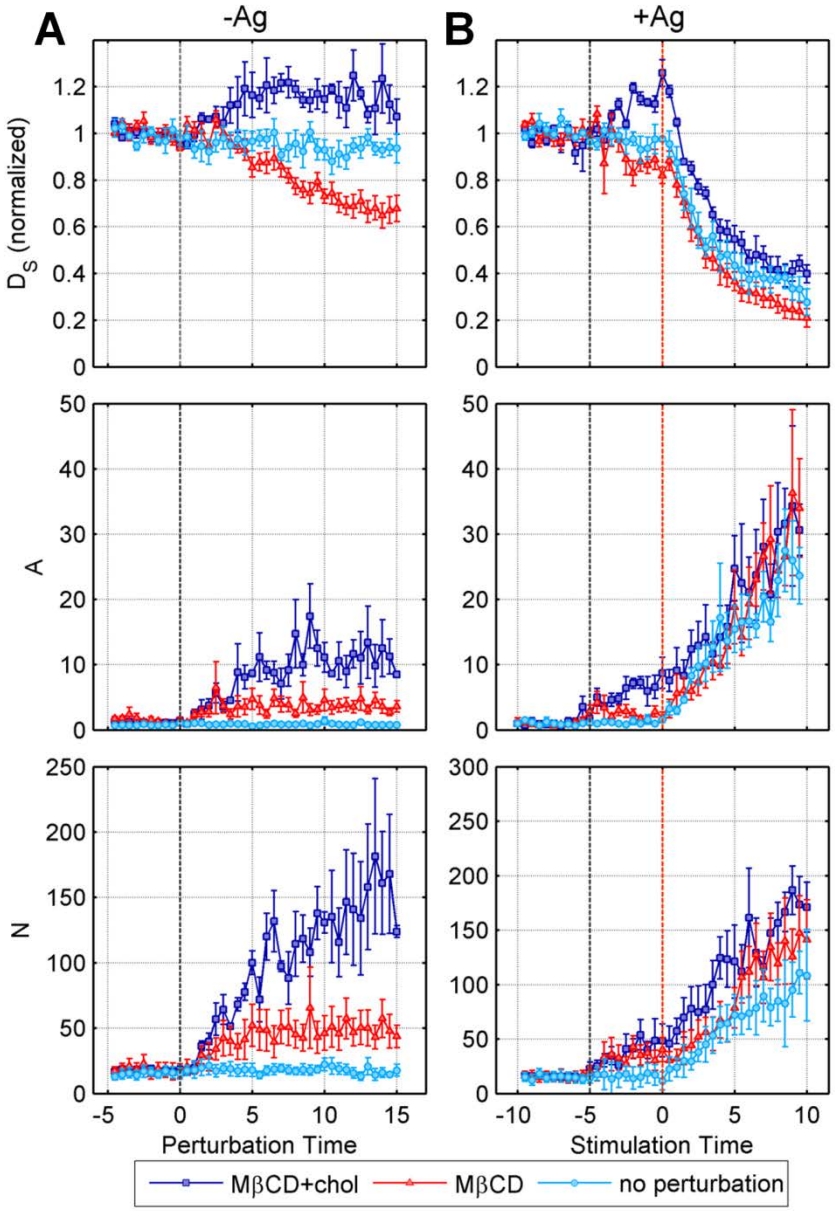

Fig. S6: Cholesterol perturbation affects average parameter values in live cell experiments. The effects of methyl-β-cyclodextrin (MβCD, red) and cholesterol-complexed methyl-β-cyclodextrin (MβCD+chol, dark blue) on average values for AF647-IgE short-time diffusion constant D_S, correlation function amplitude (A), and average number of correlated proteins (N) are measured as a function of time after the addition of the perturbation (gray dashed line). These are compared to control experiments where no perturbation is added (light blue). In (A), cells are treated with MβCD or MβCD+chol alone (or no treatment for control cells), and in (B), cells are stimulated with antigen 5 min after MβCD or MβCD+chol is added (orange dashed line), or 10 min after the start of imaging for control cells. In (A) and (B), each time trace represents the average of 4-5 independent live cell experiments. Error bars represent standard error of the mean.

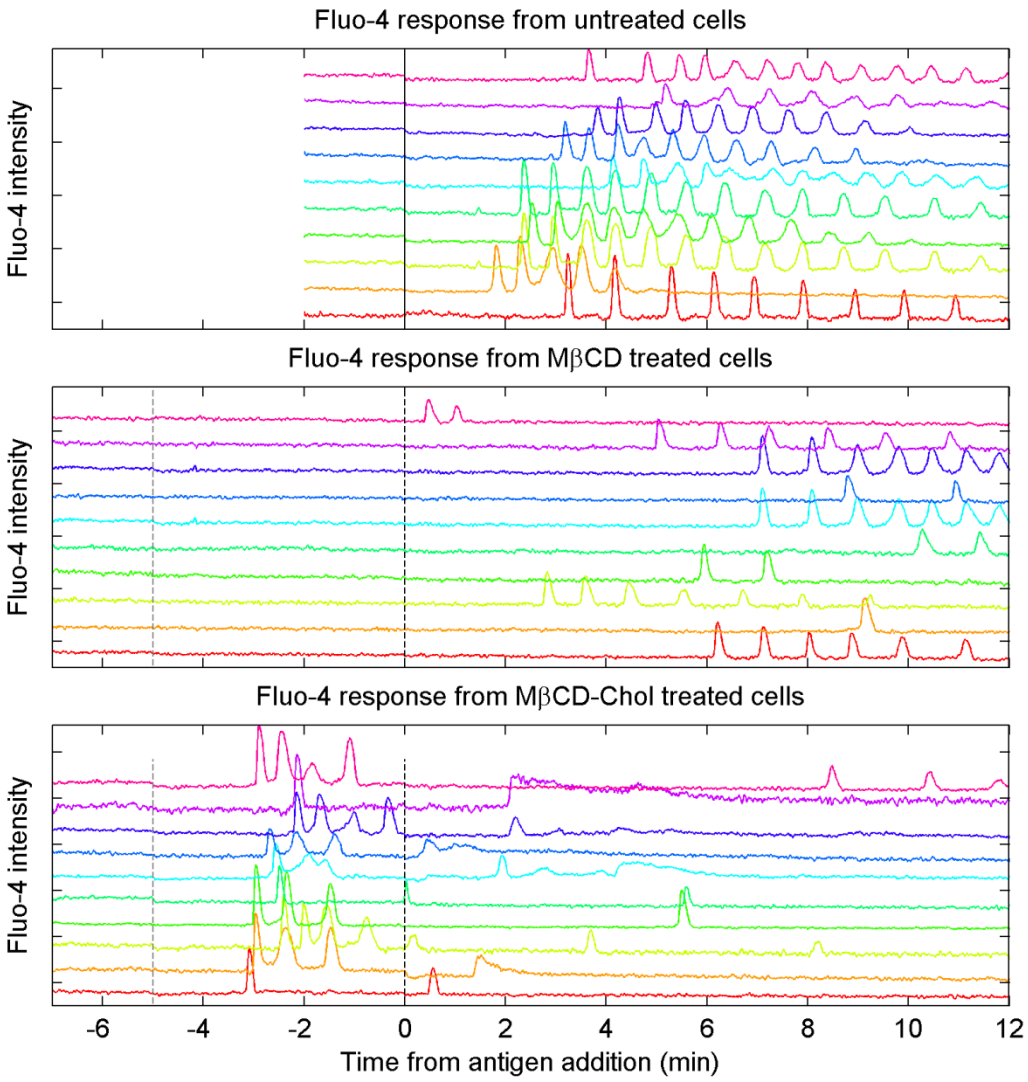

Fig. S7: The shape, frequency, and duration of Ca^{2+} oscillations are severely affected by changes in cellular cholesterol. Cytoplasmic Ca^{2+} concentrations were imaged for large fields of Fluo-4-AM loaded cells treated with MβCD (top), MβCD+chol (bottom), or neither in the case of control cells (middle), followed by stimulation with antigen as described in the Materials and Methods. Fluo-4 intensity traces are shown for representative individual cells, where intensity traces are displaced on the y axis and the y axis also delineates Fluo-4 intensity for individual cells. Traces are shown in different colors for clarity. The dotted gray line at -5 min indicates the addition of MβCD or MβCD+chol, and the dotted black line indicates the addition of 0.1µg/ml DNP-BSA.

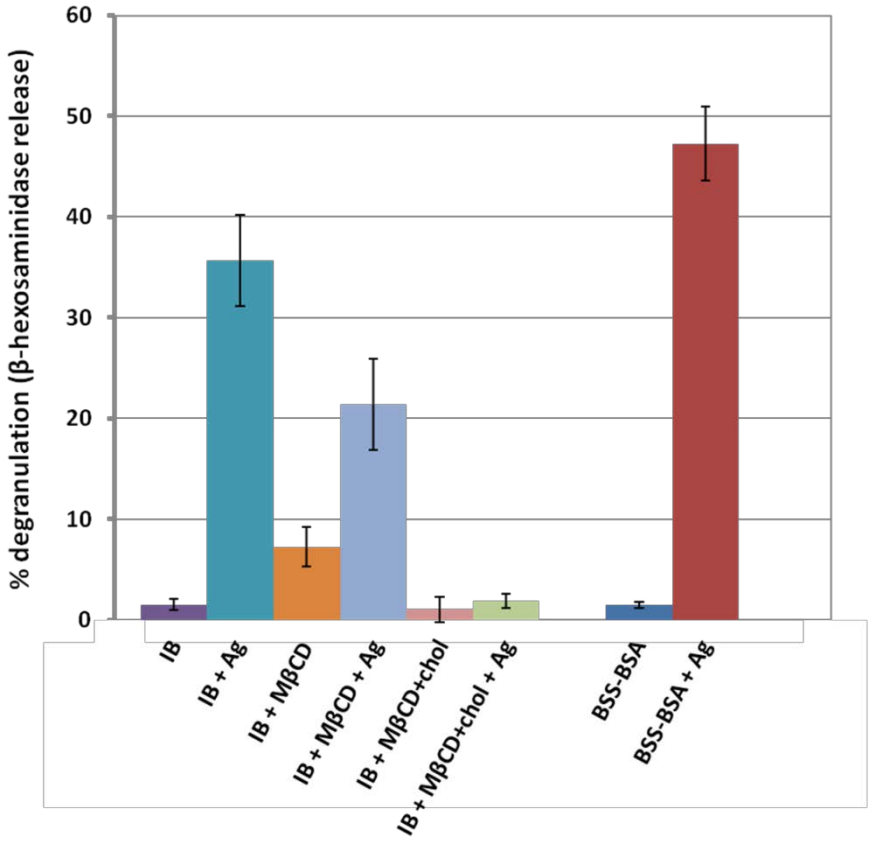

Fig. S8: Cholesterol perturbations affect the extent of antigen-stimulated degranulation as measured by β-hexosaminidase release. RBL-2H3 degranulation was measured using a β-hexosaminidase release fluorogenic assay in super-resolution imaging buffer (IB) at 37°C, with and without addition of 0.1 µg/ml DNP-BSA (Ag), and in the presence or absence of 10mM MβCD or MβCD+chol. β-hexosaminidase signal has been normalized using samples of cells lysed with TritonX-100 (TX-100) as a measure of total β-hexosaminidase content. Error bars represent standard error of the mean of multiple samples measured for each condition. Additional control samples were made in BSS + 1mg/ml BSA to test for the effect of the imaging buffer.

MATERIALS AND METHODS

Chemicals and Reagents

Amine reactive AlexaFluors 647 and 532 (AF647 and AF532), Fluo-4-AM, and Tetraspeck .125 μm fluorescent nanospheres were purchased from Life Technologies (Carlsbad, CA). β-mercaptoethanol, reduced L-glutathione, methyl-β-cyclodextrin, cholesterol-complexed methyl-β-cyclodextrin, glucose oxidase, and catalase were purchased from Sigma (St. Louis, MO). AF532 and AF647 -IgE were prepared by conjugating purified mouse monoclonal anti-2,4-dinitrophenyl (DNP) IgE with AF532 or AF647, as previously described (12, 13). AF647-IgE was measured to have a dye:protein ratio of 2.2:1. Multivalent antigen, dinitrophenyl- conjugated BSA (DNP-BSA), with an average of 24 DNP molecules per BSA was prepared as described previously (14). Glutaraldehyde (25% stock) was purchased from Ted Pella (Redding, CA). Para-formaldeyde was purchased from Electron Microscopy Services (Hatfield, PA). Cell culture supplies including MEM, Trypsin-EDTA, and gentamicin sulfate were purchased from (Life Technologies), and FBS was purchased from Atlanta Biologicals (Atlanta, GA). Cell culture dishes were purchased from MatTek (Ashland, MA).

Sample Preparation

Rat Basophilic Leukemia (RBL-2H3) cells were maintained with media containing MEM 20% FBS, 10 μg/ml gentamicin sulfate as described previously (12), then harvested using Trypsin-EDTA. MatTek Dishes were prepared with fiduciary markers by applying a dilute (1:1000 dilution in phosphate-buffered saline) solution of Tetraspeck fluorescent nanospheres to freshly oxygen plasma-cleaned wells for 15 minutes before rinsing three times with RBL-2H3 media. Cells were then plated sparsely in the dishes (0.1×10^6/well) overnight at 37°C.

Fixed cell samples:

The cells were sensitized with either AF647-labeled IgE (1μg/ml) (for single-color experiments) or a mixture of AF647-labeled IgE and AF532-labeled IgE (1μg/ml total) (for two-color experiments) in HEPES-buffered media (80% MEM, 20% fetal bovine serum, 50mg/L gentamicin, and 20mM HEPES) for 1 to 2 hours at room temperature. Dishes containing cells were rinsed and incubated in media at 37ºC for 5 minutes, rinsed again with warm PBS, treated with 1 μg/mL DNP-BSA in media (for 0,1,5, or 10 min) at 37°C, rinsed with warm PBS, and then chemically fixed (4% paraformaldehyde 0.1% glutaraldehyde in PBS) for 10 minutes at room temperature. Samples were then blocked with 2% fish gelatin, 2 mg/mL BSA in PBS for 10 minutes. For both single- and two-color experiments, fixed samples were washed 3 or more times with PBS and once with buffer containing 100mM Tris, 10mM NaCl, and 10% w/w glucose before imaging.

Live cell samples:

The cells were sensitized with AF647-labeled IgE (1μg/ml) in HEPES-buffered media for 1 to 2 hours at room temperature. Dishes containing sensitized cells were rinsed first with media, then once with super-resolution imaging buffer (IB: 30mM Tris, 135mM NaCl, 5mM KCl, 1mM $MgCl_2$, 1.8mM $CaCl_2$, 55mM glucose, 500μg/mL glucose-oxidase, 40μg/mL catalase, and 50mM glutathione at pH 8) before imaging.

Super Resolution Imaging

Imaging Setup:
Single label fixed samples were imaged on an inverted microscope (Leica DM-IRB, Wetzlar, Germany) under TIRF illumination through a 1.42 numerical aperture (N.A.) 100X Leica objective lens with a 100mW 642nm diode-pumped solid state (DPSS) laser (Crystalaser, Reno, NV) which is attenuated with neutral density filters as needed for the illumination requirements of the experiment. Typical laser power used during super-resolution data collection was about 60mW at the sample. Two-color experiments on fixed cells were conducted on an inverted Olympus IX81-ZDC microscope with a cellTIRF module (Olympus America, Center Valley, PA) under TIRF illumination though a 1.45 N.A. 100X Olympus objective lens with either a variable power 75mW 642nm DPSS laser (Coherent, Santa Clara, CA) or a 150mW DPSS 532 laser (Cobolt, Stockholm, Sweden). In both instrument setups, images were recorded with an Andor iXon 897 EM-CCD camera (Belfast, UK) using custom image acquisition code written in Matlab (The MathWorks, Natick, MA). Live cell samples were imaged on both microscopes. The camera field of view was cropped during imaging to include only a region of interest that encompasses the entire cell being imaged in order to reduce image file size and increase the camera frame rate. Camera frame rates were dependent on our exposure time of 10ms, camera settings, and the size of the cropped region of interest.

Fixed cell imaging:
Cells were imaged in the presence of an oxygen-scavenging and reducing imaging buffer (100mM Tris, 10mM NaCl, 10% w/w glucose, 500 μg/mL glucose-oxidase, 40μg/mL catalase, and 1% β-mercaptoethanol at pH 8.5). After individual cells were located using relatively low power illumination, laser power was increased to induce AF647, or AF532 photo-switching. Movies of AF647, or AF532 photo-switching were acquired with 10ms exposure time at frame rates between 25 and 32 frames per second for at least 2500 frames.

Live cell imaging:
Live cells were imaged at room temperature to limit the effects of receptor internalization during the imaging experiment. Imaging was performed in the presence of super-resolution imaging buffer (IB: 30mM Tris, 135mM NaCl, 5mM KCl, 1mM $MgCl_2$, 1.8mM $CaCl_2$, 55mM glucose, 500μg/mL glucose-oxidase, 40μg/mL catalase, and 50mM glutathione at pH 8). Live cells were imaged at room temperature with frame exposure times of 10ms and frame rates between 25 and 32 fps for at least 5 minutes before addition of DNP_{24}-BSA at a final concentration of 1μg/ml and monitored as stimulation progressed for at least 10 minutes for data reported in Figs. 1-4, S2, and S4. In experiments where antigen was competed off of surface IgE using DNP aminocaproyl-L-tyrosine (DCT), a stimulating dose of 0.1μg/ml antigen was used, and DCT at a final concentration of 20 μM was added 7 minutes after antigen addition (Fig. 5). Cells were imaged for at least 10 minutes after the addition of DCT. In membrane cholesterol perturbation experiments (Figs 6, S5, S6, S7, and S8), methyl-β-cyclodextrin (MβCD) or cholesterol-complexed methyl-β-cyclodextrin (MβCD+chol) was added at a final concentration of 10mM 5 min before the addition of either DNP-BSA at a final concentration of 0.1ug/ml or a blank addition of an equivalent volume of buffer in experiments where cells were not stimulated. In experiments when cholesterol perturbation is followed by stimulation with DNP-BSA, cells were imaged for an additional 5 minutes in the presence of MβCD or MβCD+chol before antigen was added at a final

concentration of 0.1ug/ml. The cells were then imaged for at least 10 minutes following stimulation. In experiments where cells were not stimulated after cholesterol perturbation, they were imaged for at least 15 minutes after addition of MβCD or MβCD+chol.

Image Analysis

Super-resolution image reconstruction:

Movies of AF647 or AF532 photoswitching were analyzed as described in (3). In brief, diffraction-limited spots are fit to a two-dimensional Gaussian function though least squares fitting using the built-in Matlab function *fminfunc()*. Localized probes that are outliers in spot width, brightness, aspect ratio, and 2D gaussian fit quality are excluded from the reconstructed image. In fixed cell measurements, probes that are localized in the same position in sequential frames, within twice the average localization precision, are combined. For live cell experiments, single molecule trajectories are determined as described below and only the first localization positions are included in reconstructed images. The average number of localizations that are accepted after culling and grouping is 12 per 10ms frame. For all experiments reconstructed images are assembled by incrementing a pixel value once for each time a localized signal is identified at that location. These images are then convolved with a two-dimensional Gaussian for display purposes. Super-resolution images are reconstructed from varying numbers of individual frames of raw data. For example, fixed cell images are reconstructed from at least 2500 frames (~100 s of integrated imaging time) of raw data, amounting to a total of approximately 30,000 single localizations, whereas live cell images are reconstructed from between 500 and 2000 frames (~20 and 80 s integrated imaging time), amounting to between approximately 6,000 and 24,000. The localization precision was calculated from correlation functions as described in (3) and had typical values around 20nm for a given imaging experiment using AF647 as the super-resolution probe.

Correlation function analysis of super-resolution images:

Receptor clustering in super-resolution images is analyzed using spatial auto- and cross-correlation functions. Correlation functions are calculated from reconstructed images of localized fluorophores as described previously (3). Briefly, reconstructed images (I) are masked (M) to exclude contributions from cell edges, and autocorrelation functions are tabulated using fast Fourier transforms (FFTs) according to:

$$g(r) = 1/ \rho^2 \times FFT^{-1}(|FFT(I)|^2)/ FFT^{-1}(|FFT(M)|^2)$$

where ρ is the average density of localized signals within the masked region. The autocorrelation of the mask is included to properly account for boundary conditions. A Matlab function that tabulates g(r) from images is included in Supplementary material in (3). Cross-correlation functions for fixed cell images are tabulated similarly from masked images from two distinct images I_1 and I_2 with average densities ρ_1 and ρ_2 according to:

$$c(r) = 1/(\rho_1 \rho_2) * RE(FFT^{-1}(FFT(I_1) \times FFT(I_2)^*)))/ FFT^{-1}(|FFT(M)|^2)$$

where * denotes a complex conjugate and RE() indicates the real part. Auto-correlation functions from single color live cell images were quantified as described in the main text.

Correcting for over-counting in fixed cell images:
Auto-correlation functions from single-color fixed cell images are subject to additional clustering due to over-counting of labeled proteins, and quantifications are corrected for possible over-counting as described previously (3) and summarized below. When over-counting is present in a super-resolution image, the measured auto-correlation as a function of distance r, $g_{meas}(r)$, has the form

$$g_{meas}(r) = [\delta(r)/\rho + g(r>0)]*g_{PSF}(r),$$

where here the terms in square brackets are the delta function present at r = 0 ($\delta(r)$) plus the auto-correlation arising from the real distribution of labeled protein centers at distances greater than r = 0 ($g(r>0)$). Both terms are convoluted (*) with the correlation function of the effective point spread function (PSF) of the measurement $g_{PSF}(r)$, as described in detail in (3)). ρ is the average density of labeled molecules in the analyzed area. If a Gaussian shape of the PSF is assumed, the equation becomes

$$g_{meas}(r) = \exp\{-r^2/4\sigma^2\}/(4\pi\,\sigma^2\,\rho) + g(r>0) *g_{PSF}(r)$$

where the first term represents the contribution to $g_{meas}(r)$ of over-counting. g_{PSF} is estimated by comparing the auto-correlation of images reconstructed from all identified single molecule centers to those of images reconstructed from data grouped to account for localized single molecules within a threshold of twice the localization precision and are identified in sequential frames as described previously (3). g_{PSF} is then fit to a two-dimensional Gaussian function to determine σ, and we assume a surface density of the receptor to be 200 molecules/μm^2 (4). The measured correlation function is then fit to the above equation to determine the correlation function due to the real distribution of labeled molecules. $g(r>0)$ is approximated by an exponential function, $1+Aexp(-r/\xi)$, and A and ξ are extracted as fit parameters.

Cross-correlation functions from two-color experiments do not contain additional contributions from over-counting and can be fit to a single filtered exponential function to extract clustering parameters. Measured cross-correlations are of the form:

$$g_{meas}(r) = g_{PSF}(r)*g(r>0)$$

where $g(r>0)$ represents the correlation function arising from the real distribution of labeled molecules at distances greater than r = 0 and $g_{PSF}(r)$ is a function that applies a Gaussian filter with width proportional to the resolution of the image and represent the PSF of the measurement. $g(r>0)$ is well fit by a single exponential function, yielding

$$g_{Fit}(r) = g_{PSF}(r)*[1+ (Aexp(-r/\xi))]$$

where A and ξ are extracted as fit parameters.

Single particle tracking and diffusion analysis:

Single receptor trajectories are generated from fluorophore locations recorded within a masked area in live cell experiments using a simple tracking algorithm, in which localized probes in successive frames are linked in a trajectory if a localization in one frame falls within some maximum distance (here, 400-500nm) of a localization in the previous frame. This maximum step size is chosen by examining the resultant step size distribution and ensuring that it follows a log normal distribution. If a probe localization in one frame could be linked to more than one localization in the previous frame, i.e. the tracks merge, then the merged tracks are terminated to avoid artifacts. Also, if a point cannot be linked to the previous frame, the algorithm will look back up to several time points (3) to compensate for fast blinking of fluorophores or single molecules lost in image processing. Similar results were obtained with more complicated tracking algorithms that perform global minimizations (15).

Mean squared displacement (MSD) as a function of time interval τ is calculated over all trajectories that persist longer than two frames from the positions as a function of time (x(t) and y(t)). In general, the MSD in 2 dimensions is defined as

$$MSD(\tau) = \langle (x(t+\tau) - x(t))^2 \rangle + \langle y(t+\tau) - y(t))^2 \rangle$$

where the angled brackets denote an average over all t. MSD curves are tabulated for individual trajectories, or over all segments acquired in a single cell over a specified time window (typically 500 frames). Diffusion coefficients for individual molecules are only reported if trajectories extend at least some minimum number of frames (typically 14). Short and long time diffusion coefficients are determined through a weighted linear least squares fitting routine in Matlab (lscov), where weights were the inverse standard error of the mean for each MSD(τ).

In Figure 4D, we generate three dimensional histograms from single trajectory data by keeping track of the average diffusion coefficient (D_S) for single tracks, and the average density of receptors along each trajectory. The average density along the trajectory is determined by first reconstructing a super-resolution image from the first point of all trajectories localized within a 1000 frames (40 s) of acquired raw data. For Figure 4D, this image had a pixel dimension of 20nm by 20nm, and after reconstruction the image was convolved with a Gaussian filter with half-width of 40nm. This intensity image is then normalized so that the total average surface density is maintained at 200/μm^2. Finally, long trajectories were placed upon this image and the pixel value at each localized point along the trajectory was averaged. The three dimensional histogram was constructed by binning in both diffusion coefficient and average intensity. Histograms were filtered with a Gaussian function with half-width ≤1bin in order to smooth contours.

Ca^{2+} mobilization measurements:

RBL-2H3 cells were plated in 35mm dishes and allowed to adhere at 37 °C overnight. Cells were then sensitized with 1ug/ml unlabeled IgE for at least 2h at 37 °C prior to imaging. The cells were rinsed then labeled with the Ca^{2+}-sensitive dye Fluo-4-AM by incubating in 0.4µg of dye in 1ml of BSS containing 1mg/ml BSA (BSS-BSA) for 10min at room temperature. Cells were rinsed again to remove excess dye and imaged immediately in either BSS-BSA or in imaging buffer (IB) used for super-resolution experiments at room temperature. Fluo-4 fluorescence intensity was imaged at 2 fps under 10x

magnification. Samples were monitored as the cells were stimulated by addition of either 1 or 0.1 μM DNP-BSA 5 minutes after the start of imaging. To test the effects of cholesterol perturbation on cellular Ca^{2+} responses, MβCD or MβCD+chol was added to the dish 5 minutes after the start of imaging at a final concentration of 10mM and allowed to incubate for 5 minutes before cells were stimulated with 0.1 μM DNP-BSA as above. Fluo-4 intensity for each cell was determined by recording the average fluorescence intensity within a circle of radius 5 pixels (7.25μm) from the localized cell center as a function of time. The time averaged fractional intensity is normalized to 1 for each cell prior to treatments, and signals from at least 500 cells are averaged to obtain the average intensity traces shown in Figs. 3, 7, and S1. Small reductions in average Fluo-4 intensity vs. time due to bleaching and/or dye leakage were corrected for by fitting any downward slope present in the average Fluo-4 intensity curve within the first five minutes of imaging, prior to stimulation or addition of perturbation. The average intensity curve for all time points is then normalized by this fit. For cumulative curves of Ca^{2+} mobilization initiation events, individual cells are defined as having initiated a Ca^{2+} response if their intensity increases by a factor of 2.5 more than the average intensity of the cell prior to treatments.

Degranulation experiments:

To test the effects of imaging buffer on RBL degranulation, cells were sensitized with unlabeled anti-DNP IgE at a final concentration of 1μg/mL and plated at a density of 0.5 X 10^6 cells per well in a 96-well plate overnight at 37 °C. Adherent cells were washed in BSS-BSA and then washed into either BSS-BSA, live cell imaging buffer (IB) without a reducing agent or oxygen scavenging enzymes (135mM NaCl, 5mM KCl, 1mM $MgCl_2$, 1.8mM $CaCl_2$, 55mM glucose, 30mM Tris, at pH 8), or complete imaging buffer which includes reducing agents and oxygen scavenging enzymes (135mM NaCl, 5mM KCl, 1mM $MgCl_2$, 1.8mM $CaCl_2$, 55mM glucose, 30mM Tris, at pH 8 *with* 500μg/mL glucose-oxidase, 40μg/mL catalase, and 10, 50 or 100 mM glutathione or 10 mM β-mercaptoethanol at pH 8). After the addition of multivalent ligand DNP_{24}-BSA at 1ug/ml final concentration , the cells were incubated at 37°C for an hour, and the supernatants were taken from each well to assay the extent of β -hexosaminidase release from the cells as previously described (1). Stimulated degranulation is expressed as a percentage of the total cellular β-hexosaminidase activity present in cell lysates after solubilization in 0.1% Triton X-100.

To test the effects of cholesterol perturbations on RBL-2H3 degranulation, cells were plated and sensitized with unlabeled IgE in the same manner as above. After washing with BSS-BSA, cells were washed into BSS-BSA, complete IB, or complete IB containing 10mM MβCD or MβCD+chol. Following a 5 min incubation, DNP-BSA was added to some samples at .1ug/ml final concentration and the samples were incubated at 37°C for one hour. β-hexosaminidase released was assayed as above.

SUPPORTING REFERENCES

1. Naal, R.M.Z.G., J. Tabb, D. Holowka, and B. Baird. 2004. In situ measurement of degranulation as a biosensor based on RBL-2H3 mast cells. Biosens. Bioelectron. 20: 791–796.

2. Veatch, S.L., E.N. Chiang, P. Sengupta, D.A. Holowka, and B.A. Baird. 2012. Quantitative nanoscale analysis of IgE-FcεRI clustering and coupling to early signaling proteins. J. Phys. Chem. B. 116: 6923–6935.

3. Veatch, S.L., B.B. Machta, S.A. Shelby, E.N. Chiang, D.A. Holowka, et al. 2012. Correlation functions quantify super-resolution images and estimate apparent clustering due to over-counting. PloS One. 7: e31457.

4. Erickson, J., B. Goldstein, D. Holowka, and B. Baird. 1987. The effect of receptor density on the forward rate constant for binding of ligands to cell surface receptors. Biophys. J. 52: 657–662.

5. Machta, B.B., S. Papanikolaou, J.P. Sethna, and S.L. Veatch. 2011. Minimal Model of Plasma Membrane Heterogeneity Requires Coupling Cortical Actin to Criticality. Biophys. J. 100: 1668–1677.

6. Andrews, N.L., K.A. Lidke, J.R. Pfeiffer, A.R. Burns, B.S. Wilson, et al. 2008. Actin restricts FcεRI diffusion and facilitates antigen-induced receptor immobilisation. Nat. Cell Biol. 10: 955–963.

7. Sheets, E.D., D. Holowka, and B. Baird. 1999. Critical Role for Cholesterol in Lyn-mediated Tyrosine Phosphorylation of FcεRI and Their Association with Detergent-resistant Membranes. J. Cell Biol. 145: 877–887.

8. Surviladze, Z., L. Dráberová, M. Kovářová, M. Boubelík, and P. Dráber. 2001. Differential sensitivity to acute cholesterol lowering of activation mediated via the high-affinity IgE receptor and Thy-1 glycoprotein. Eur. J. Immunol. 31: 1–10.

9. Yamashita, T., T. Yamaguchi, K. Murakami, and S. Nagasawa. 2001. Detergent-resistant membrane domains are required for mast cell activation but dispensable for tyrosine phosphorylation upon aggregation of the high affinity receptor for IgE. J. Biochem. (Tokyo). 129: 861–868.

10. Kato, N., M. Nakanishi, and N. Hirashima. 2003. Cholesterol depletion inhibits store-operated calcium currents and exocytotic membrane fusion in RBL-2H3 cells. Biochemistry (Mosc.). 42: 11808–11814.

11. Silveira e Souza, A.M.M., V.M. Mazucato, R.O. de Castro, F. Matioli, P. Ciancaglini, et al. 2008. The α-galactosyl derivatives of ganglioside GD1b are essential for the organization of lipid rafts in RBL-2H3 mast cells. Exp. Cell Res. 314: 2515–2528.

12. Gosse, J.A., A. Wagenknecht-Wiesner, D. Holowka, and B. Baird. 2005. Transmembrane Sequences Are Determinants of Immunoreceptor Signaling. J. Immunol. 175: 2123 –2131.

13. Larson, D.R., J.A. Gosse, D.A. Holowka, B.A. Baird, and W.W. Webb. 2005. Temporally resolved interactions between antigen-stimulated IgE receptors and Lyn kinase on living cells. J. Cell Biol. 171: 527–536.

14. Hardy, R.R. 1986. Handbook of Experimental Immunology. 4th ed. Oxford, UK: Blackwell Scientific Publication.

15. Jaqaman, K., D. Loerke, M. Mettlen, H. Kuwata, S. Grinstein, et al. 2008. Robust single-particle tracking in live-cell time-lapse sequences. Nat. Methods. 5: 695–702.